



Applied Physics Laboratory

University of Washington

1013 NE 40th Street
Box 355640
Seattle, WA 98105-6698

206-543-1300
FAX 206-543-6785
www.apl.washington.edu

27 March 2013

To: Dr. Robert Headrick, Code 322
Office of Naval Research
875 N. Randolph St.
Arlington, VA 22203-1995

From: David Dall'Osto

Subj: ONR Grant # N00014-08-1-0297, "Graduate traineeship with focus on mid-frequency environmental and acoustic measurements from SW06 (SRA-GTA)"

Encl: (1) "Elliptical acoustic particle motion in underwater waveguides," by David R. Dall'Osto and Peter H. Dahl, with attached SF298.
(2) "Properties of the acoustic intensity vector field in a shallow water waveguide," by David R. Dall'Osto, Peter H. Dahl, and Jee Woong Choi, with attached SF298.
(3) List of all presentations and publications completed over the life of the subject grant.

The attached enclosures constitute the final technical report for grant # N00014-10-1-0394. The report also contains documentation for all other publications and presentations produced during the life of the subject grant.

Regards,

Peter H Dahl
for

David Dall'Osto

cc: Administrative Grants Officer, ONRRO Seattle
Grant & Contract Administrator, APL-UW
Office of Sponsored Programs, UW
Naval Research Lab, Code 5596
Defense Technical Information Center

Elliptical acoustic particle motion in underwater waveguides

David R. Dall'Osto and Peter H. Dahl

*Mechanical Engineering and Applied Physics Laboratory, University of Washington
1013 NE 40th St. Seattle, WA 98105*

(Dated: March 22, 2013)

The degree of circularity is a vector quantity relating to the acoustic particle motion induced in an acoustic field, and is formulated by measurements of the acoustic particle velocity or the complex vector intensity. It characterizes the ellipticity of the particle motion path that, for example, can arise when there is interference between a source signal and its reflections. In an ocean waveguide the spatial dependence of this vector property depends on the water column sound-speed, surface conditions and bottom properties, in addition to the source/receiver geometry. In waveguides with nearly horizontal boundaries, the vertical component of the instantaneous intensity can be used to provide an approximation to the degree of circularity. This approximation, applied to acoustic pressure measurements from two closely spaced hydrophones made in 2006 off the New Jersey coast in waters 80 m deep, is used to invert for environmental parameters of the sediment structure.

PACS numbers: 43.30.Yj, 43.30.Ma, 43.30.Xm, 43.58.Fm

I. INTRODUCTION

In shallow water it is common to observe modulations in the amplitude and phase of the pressure field due to interference of an acoustic signal with reflections from the sea-surface and sea-bed. Hydrophones, which provide measurements of the acoustic pressure field, are commonly used to interpret these modulations using pressure-based processing schemes for source-localization, such as beam-forming with an array of hydrophones, and geo-acoustic inversion. Vector sensor measurements, which include the acoustic pressure and the three orthogonal components of the acoustic particle velocity, have been utilized in pressure-based processing schemes for source localization¹ as well as geo-acoustic characterization.² For example, the magnitude and direction of the particle velocity vector can be readily translated to the spatial dependence of the pressure phase for use in beam-forming algorithms.³

Additional vector information can be extracted from the phase relationship between the individual components of particle velocity; this phase relationship describes a fundamental property of the fluid particle motion, referred to as the degree of circularity. The degree of circularity, which can be formulated from measurements of the acoustic particle velocity or the complex intensity, is a non-dimensional number that takes on characteristic values between -1 and 1 when a signal interferes with its reflections.⁴ The direction of the particle velocity vector does not necessarily fall on a straight line (equivalent to the zero value for the degree of circularity) as the particle velocity components of interfering wavefronts do not necessarily have the same phase dependence. In ocean waveguides, the horizontal surfaces cause a phase modulation of the vertical component of the particle velocity with resulting elliptical particle motion in the vertical plane. This elliptical motion in the vertical plane can be approximated by vertical line array of closely spaced pressure sensors.

We demonstrate in this paper how the degree of circu-

larity provides a useful metric to analyze the propagation of a sound pulse in underwater waveguides. The degree of circularity has a spatial pattern that relates directly to multi-path interference. The pattern due to the multi-path interference depends on the frequency, acquisition geometry, bottom properties and water column properties. Spatially distributed measurements of the degree of circularity can be used to determine the depth and range of sources, and reflections from sub-bottom layers cause a distinct pattern in range and depth which can be used for geo-acoustic inversion. Geo-acoustic parameters of a layered seabed from the Shallow Water 2006 (SW06) experiment near the New Jersey coastline, which has been well characterized,^{5-7,9} are presented in light of this vector property. An inversion scheme based on the range dependence of the degree of circularity is presented along with the sensitivity to specific geo-acoustic parameters.

The paper is organized as follows: Section II establishes the mathematical formulation for the degree of circularity from particle velocity measurements, complex intensity measurements, and an approximate degree of circularity from one directional component of the complex intensity. Section III demonstrates the effect of the source-receiver positions on the degree of circularity, illustrated by an analytical formulation of the characteristic Lloyd's Mirror interference pattern caused by a source below a pressure-release surface. A laboratory experiment approximating this field demonstrates the observability of the frequency and spatial dependence of the degree circularity. Section IV demonstrates how the degree of circularity is affected by reflections from layered boundaries. Experimental data from the SW06 experiment, from which an approximate degree of circularity is formulated by vertical pressure measurements, are used to identify properties of the sediment layering structure. Parabolic equation (PE) simulations are presented to demonstrate the spatial properties of the degree of circularity. Section V presents a parameterized geo-acoustic model of the degree of circularity for the SW06 site to demonstrate the sensitivity to environmental parameters

in terms of the Cramer Rao Lower Bound (CRLB). A geo-acoustic inversion of the SW06 site based on experimental measurements of the degree of circularity is also presented. Section VI provides a summary of the results.

II. THE DEGREE OF CIRCULARITY, Θ

A. Θ computed via particle velocity, \mathbf{v}

The magnitude and phase relationship among the individual components of the complex particle velocity, v_i , can be used to construct a vector quantity, the degree of circularity,

$$\Theta = 2 \frac{\text{Im}(\mathbf{v} \times \mathbf{v}^*)}{|\mathbf{v}|^2} \quad (1)$$

where \times is the cross product, the asterisk is the complex conjugate, and the factor of 2 sets the bounds of any component of Θ between ± 1 . Each vector component of Θ quantifies the degree to which the particle motion, projected on three orthogonal planes, resembles a circle.

When any two components of the particle velocity are locked in phase, the particle motion in the plane of the two corresponding axes falls on a straight line. The component of Θ describing this motion will be perpendicular to this plane, and for this straight-line motion it is equal to zero as a result of the cross product. This is exemplified by a single plane wave propagating in the x-y plane where the z-component of Θ equals 0.

If two components of particle velocity are not locked in phase, the motion is elliptical. The component of Θ describing this elliptical motion is between 0 and ± 1 , where purely circular motion is ± 1 . This can occur in acoustic fields characterized by multi-path interference, such as that of a plane-wave and its reflection from a boundary. The sign of Θ determines the direction in which a particle moves about the path with respect to the fixed coordinate axis. Positive valued Θ represents counterclockwise motion and negative valued Θ represents clockwise motion. This distinction is further clarified in Sec. III by an analytic and experimental example involving the Lloyd mirror interference effect.

B. Θ computed via complex intensity, \mathbf{I}_c

The degree of circularity, Θ , can be derived from the complex intensity vector, \mathbf{I}_c . This allows for an approximation based on measurements of only one component of particle velocity, which is explained subsequently. The complex intensity, which describes the instantaneous energy flux, is formulated by,

$$\mathbf{I}_c(t) = \frac{1}{2} p(t) \mathbf{v}(t)^* = \mathbf{I}(t) + i\mathbf{Q}(t), \quad (2)$$

where p is the acoustic pressure, and the real and imaginary parts of \mathbf{I}_c represent the time varying amplitude of the active (\mathbf{I}) and reactive (\mathbf{Q}) intensity, respectively.¹⁰ For a steady state acoustic field, \mathbf{I}_c is time-independent.

An alternative formulation of Θ (equivalent to Eq. 1) based on the complex intensity is,

$$\Theta = 2 \frac{\mathbf{I} \times \mathbf{Q}}{|\mathbf{I}|^2 + |\mathbf{Q}|^2}, \quad (3)$$

Note that reactive intensity is very closely linked to elliptical particle motion: when $|\mathbf{Q}| = 0$, the degree of circularity is zero; when $|\mathbf{Q}| > 0$, the sign of the reactive intensity relates directly to the particle motion polarization.

C. Approximation of Θ component in the vertical plane

The sound fields discussed here are assumed to exhibit azimuthal symmetry (i.e. the particle motion lies only in the vertical plane). Only one component of the vector $\Theta = [\Theta_r, \Theta_z, \Theta_\theta]$ in cylindrical coordinates is non-zero, the component perpendicular to the r-z plane (Θ_θ). Henceforth, for azimuthally symmetric fields we will drop the vector notation and simply denote the circularity as Θ .

An approximation to Θ in the vertical plane can be derived from two vertically separated hydrophones. This approximation relies on an accurate estimate of the complex horizontal intensity. The horizontal active intensity can be estimated by vector subtraction of the vertical component of active intensity from the total active intensity. The total active intensity can be approximated directly from the pressure measurements as the pressure magnitude squared divided by the characteristic impedance, $\rho_0 c$, (or plane wave intensity). The resulting approximate horizontal active intensity is

$$\tilde{I}_r = \sqrt{\left(\frac{|p|^2}{\rho_0 c}\right)^2 - I_z^2}, \quad (4)$$

where I_z is the vertical intensity, and the tilde indicates an approximate of the horizontal intensity, I_r .

As a word of caution, in regions of strong destructive interference, the magnitude of the total active intensity may be underestimated by the plane wave intensity. This is often encountered in shallow water, where the multiple upward and downward propagating waves set up standing waves in the vertical direction. In regions of complete destruction the magnitude of the vertical component of particle velocity can exceed the magnitude of pressure divided by $\rho_0 c$. Measurements in these regions may have a negative value under the square root in Eq. 4, resulting in an imaginary component of active intensity, an apparently nonsensical result. Although the approximation breaks down, the ratio of the vertical intensity component to the plane wave intensity serves as an indicator of dislocations, or nulls, in the field. In these cases, this ratio serves as a field indicator which can be used to determine the spatial pattern of nulls, which in shallow water are highly dependent on the modes of the waveguide.¹⁰

The approximation of total intensity used in Eq. 4 is appropriate as long as the interfering waves do not cause complete destructive interference, i.e. waves traveling in

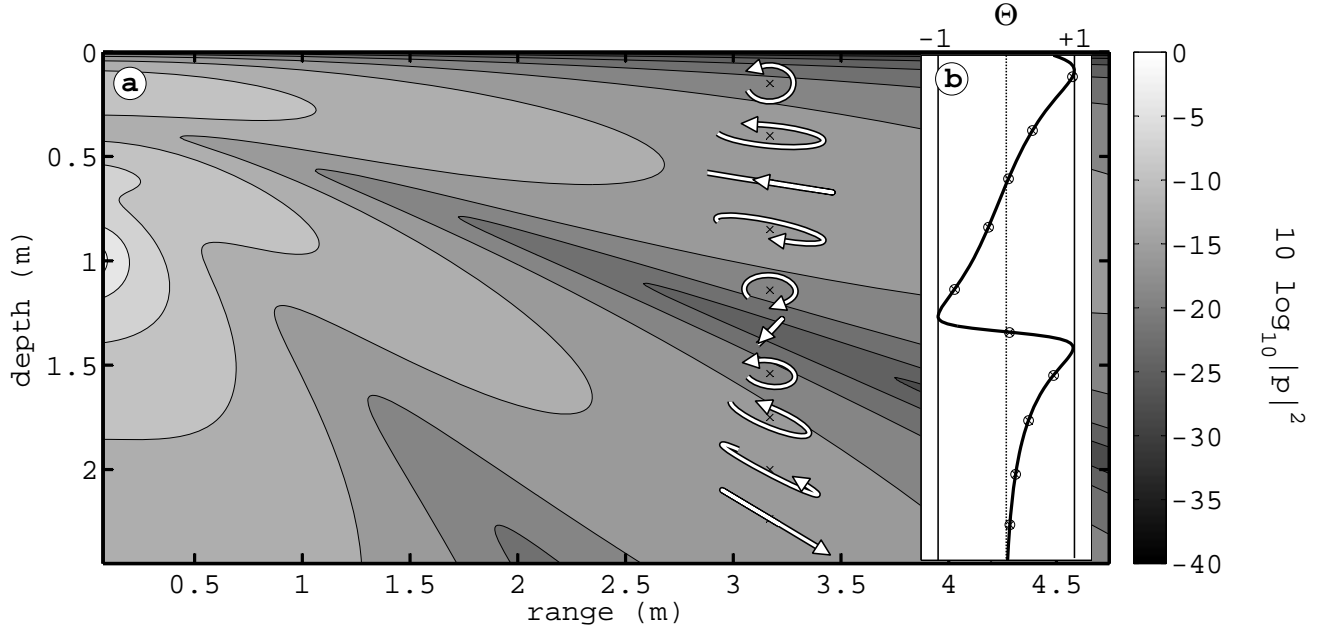


FIG. 1. (a) 3 dB contour intervals of the pressure magnitude, relative to the level at 1 m, due to a 2000-Hz point source 1 m below the air-water interface. Exaggerated particle paths at a range of 3.17 m and 10 depths are shown, for which Θ ranges from linear ($\Theta = 0$) to circular ($\Theta = \pm 1$). (b) Θ as a function of depth at the range, 3.17 m. The dots correspond to the discrete particle depths depicted in (a).

the same direction (e.g. upward or downward). If upward and downward traveling waves interference, they can completely annihilate each other and cause a dislocation where $|p|/|v| \neq \rho_0 c$. Furthermore, the horizontal component of reactive intensity, Q_r , is virtually zero a few wavelengths from the source, i.e. when $kr \gg 1$, where k is the acoustic wavenumber and r is the slant range to the source. Substituting \tilde{I}_r and $\tilde{Q}_r = 0$ for the appropriate quantities in Eq. 3, the approximate

$$\tilde{\Theta} = \frac{Q_z \tilde{I}_r}{I_z^2 + \tilde{I}_r^2 + Q_z^2}, \quad (5)$$

captures the dominate features of the true Θ , where the tilde indicates an approximate measure of circularity. Most importantly, $\tilde{\Theta}$ can be formed from two closely spaced ($< \lambda/4$) hydrophones, extending this analysis of particle motion to observations made by a vertical line array of hydrophones. Note that the accuracy of the approximate $\tilde{\Theta}$, as computed by two hydrophones, is dependent not only on the accuracy of the finite-difference estimate of particle velocity, but also the accuracy of the assumption that $|p|/|v| = \rho_0 c$.

III. EFFECTS OF SOURCE POSITION AND FREQUENCY ON Θ

Consider an underwater sound source located close to the sea surface. The pressure field of a tone source exhibits the characteristic Lloyd's mirror interference pattern, which has a straight forward analytical solution. The pressure field is the sum of two point sources, one

at the source depth and the other (a virtual source representing the reflection) equidistant from, but on the opposite side of, the pressure release surface. The pressure field is given by

$$p(x, y; t) = p_0 \frac{e^{-ikr_1} e^{i\omega t}}{r_1} - p_0 \frac{e^{-ikr_2} e^{i\omega t}}{r_2}, \quad (6)$$

where $r_1 = \sqrt{(x - x_0)^2 + (y - y_0)^2}$,
and $r_2 = \sqrt{(x - x_0)^2 + (y + y_0)^2}$,

and where $[x, y]$ are the horizontal range and depth of the field point, $[x_0, y_0]$ is the position of the source, ω is the angular frequency, and p_0 represents the source level (with units pressure times distance). The reflection coefficient, which modifies the second term (virtual source), is -1 due to the pressure release boundary condition. This assumption is reasonable at the frequencies (> 2000 Hz) and source depth (1 m) used in this demonstration. (A point source with $kz_0 \ll 1$, where z_0 is the source depth, can radiate a significant portion of energy across the air-water interface, a phenomenon referred to as transparency;¹¹ the values of kz_0 considered here are all greater than 1.)

The acoustic particle velocity field is related directly to the pressure field by conservation of momentum,

$$\frac{d\mathbf{v}(t)}{dt} = -\frac{1}{\rho_0} \nabla p(t), \quad (7)$$

where ρ_0 is the ambient density of the medium.

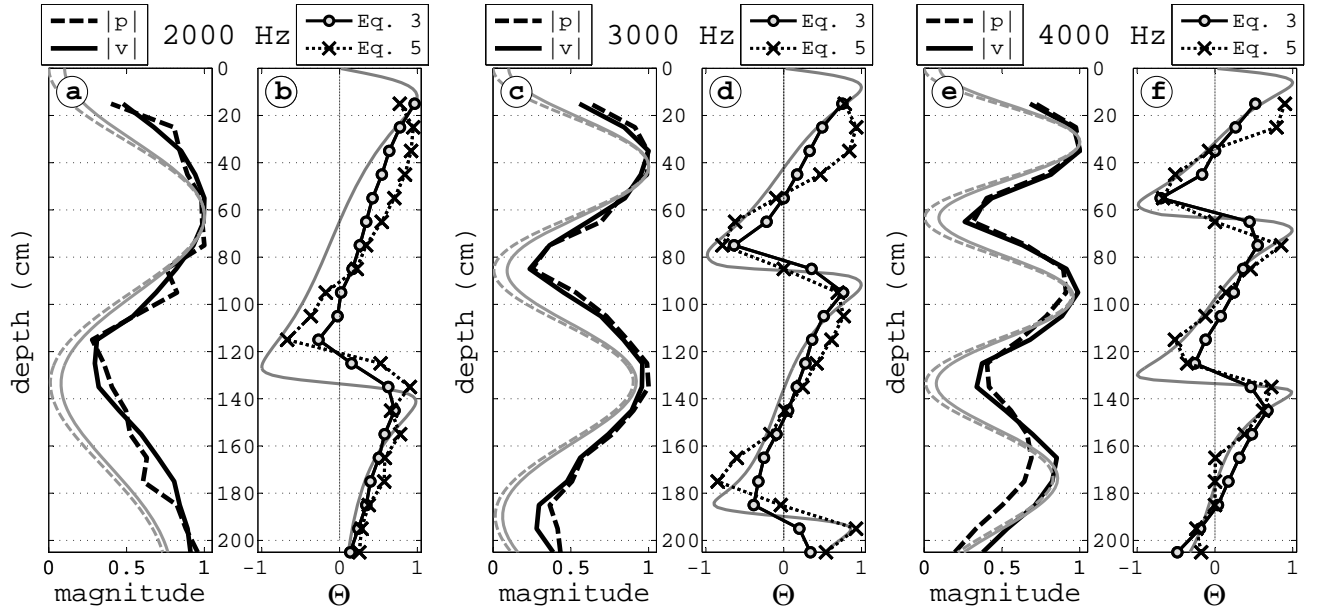


FIG. 2. (a) Experimental measurements of pressure magnitude $|p|$ (solid black) and particle velocity magnitude $|v|$ (dashed black) versus depth at 2000 Hz are along with the analytic solution of $|p|$ (solid gray) and particle velocity magnitude $|v|$ (dashed gray). Each profile is normalized by the maximum value. (b) Experimental measurements of the true circularity Θ (circle's) and the approximate $\tilde{\Theta}$ (x's) computed from the vertical component of intensity are plotted over the analytic model of Θ (gray). Results are repeated in (c) and (d) at 3000 Hz, and in (e) and (f) at 4000 Hz.

A. Analytical depth dependence of Θ

The interference pattern of Lloyd's mirror is dependent on both the source depth and frequency. Figure 1 shows 3 dB contours of the pressure magnitude field (relative to the maximum) for a 2000 Hz tone source at depth 1 m. The arrows in Fig. 1 show the path (highly exaggerated) that fluid particles at a range 3.17 m and 10 representative depths follow over 3/4 of a cycle. These paths are exaggerated by the same factor to preserve their relative magnitudes (actual displacements are $\mathcal{O}(10^{-11})$ m for a source level of 120 dB re $1\mu\text{Pa}$ @ 1 m).

The depth dependence of Θ is shown in the inset of Fig. 1. At the depths 0.65 m and 2.25 m, the particle motion (and thus particle velocity) falls on a line oriented with the ridge of constructive interference. A similar straight line path occurs at the trough of destructive interference at 1.33 m, but here the line is oriented in the direction perpendicular to the trough of destructive interference. Particle motion that does not fall on a straight line is observed on either side of the straight line regions. The motion here is best described as elliptical.

As a reminder, the acoustic particle motion falls between two extremes as parameterized by Θ , purely circular motion when $\Theta = \pm 1$ and motion falling along a line when $\Theta = 0$. The sign of Θ signifies the direction of travel, or polarization, of the particle motion. Note that above or below a position with zero circularity, the polarization abruptly changes from clockwise to counterclockwise. For example, at 1.13 m Θ is negative (clockwise) and at 1.53 m it is positive (counterclockwise).

The sign-change on either side of a point with zero

circularity can be also be thought of as indicating either prograde or retrograde motion. Prograde motion occurs when the particle motion directly above and below a point of zero circularity converge and travel in the same direction as the energy propagation. Prograde motion occurs along crests of constructive interference. Conversely, retrograde motion occurs near destructive interference, evidenced by converging particle motion directly above or below travels in the opposite direction of energy propagation. The divergence (or convergence) of the reactive intensity can be used to qualify either prograde (divergent $\nabla \cdot \mathbf{Q} > 0$) or retrograde (convergent $\nabla \cdot \mathbf{Q} < 0$) motion. Examples of divergent (and convergent) reactive intensity in ocean waveguides, and how they relate to dislocations in the field, can be found in Dall'Osto, et al.¹⁰

Abrupt changes in the sign of Θ are readily observable in experimental measurements as is discussed next. Furthermore, the depth spacing of these transitions (and their frequency dependence) has implications in source depth and ranging. Although not developed here, these abrupt transitions relate directly to the interference pattern, which can identify the spatial structure of the interference used in source depth inversion algorithms.⁸

B. Experimentally measured depth dependence of Θ

These same particle motion features predicted by the analytic solution (Fig. 1) have been observed experimentally at the University of Washington Applied Physics Laboratory's acoustic test facility (ATF). An approxi-

mation to Lloyd's Mirror was generated by an acoustic projector (USRD standard type F37 transducer) positioned at depth 1 m. Three pulses at center frequencies 2, 3, and 4 kHz, each of 4 ms duration, were recorded by an epoxy encased tri-axial accelerometer (model VHS-100 from Ocean Applied Acoustic-Tech, China).

The accelerometer was suspended in a frame by mechanical springs to decouple the device from the frame and to maintain its orientation. Two pressure-sensing hydrophones, spaced 15 cm apart, were attached to the frame directly above and below the accelerometer. The frame was attached to a vertical profiler that moved the sensor in 10 cm depth increments. To recreate Lloyd's Mirror, the received signal was gated to include only the first 1 ms of interference between the direct and surface arrival; after 1 ms, additional unavoidable reflections in the ATF (e.g. pontoons, lake bottom) complicate the interference pattern. At each depth increment Θ is calculated by Eq. 1, and $\tilde{\Theta}$ by Eq. 5. To compute the complex intensity for the circularity calculations, the pressure at the center of the accelerometer was approximated by the average of the two hydrophone signals.

Figure 2a, c, and e show the experimentally measured magnitude of the pressure (solid black) and particle velocity (dashed black) plotted relative to their maximum recorded level at 2, 3, and 4 kHz, respectively. These data follow the same depth dependence as the analytic solution given in Eq. 6 for the pressure (solid gray) computed and the particle velocity (dashed gray).

Figure 2b, d, and f show the measured true Θ (circle's) and approximate $\tilde{\Theta}$ (x's) for 2, 3, and 4 kHz, respectively. These measurements agree with the analytic model of Θ (gray), as they exhibiting either a slowly changing circularity though maxima in the field or an abrupt change in sign at the destructive nodes. The depths of these features are related directly to the frequency of the signal, and the depth and range of the source.

The distinct advantage of the Θ description over the pressure or particle velocity magnitude, is the ability to distinguish the proximity and direction of a maxima/node from one measurement point. That is, on either side of a null or maximum, the pressure field will appear to have the same magnitude while the value of Θ will be of opposite sign. A change in the sign of Θ from one to the other suggests passing through a minimum (or maximum) while equivalent pressure magnitude measurements may indicate a constant pressure level. Additionally, since Θ is non-dimensionalized with respect to the source level, analysis based on Θ is not sensitive to source level fluctuations. This applies equally to $\tilde{\Theta}$ derived completely from the particle velocity (Eq. 1) or intensity measurements (Eq. 3).

IV. EFFECTS OF A LAYERED SEABED ON Θ

For a source close to the water-sediment interface, a similar Lloyd's mirror pattern (as discussed in the previous section) can be observed. Unlike the sea-surface reflection, where little energy is transmitted through the air-sea interface, a portion of the energy incident on the

TABLE I. Models of the sediment layer above the R-reflector, for nominal location 39.0245 N, 73.0377 W. The layer is parameterized by the thickness, H_s , and soundspeed, c_s . Two values indicate models with multiple overlaying sediment layers, the bottom layer (R-reflector) is modeled as a half-space with soundspeed 1740 m/s. Broadband PE simulations are used to compare the various sediment models in terms of the characteristic wavelength of the interference pattern, λ_Θ . The data show $\lambda_\Theta \simeq 16$ m.

Soundspeed (c_s)	Thickness (H_s)	$\lambda_\Theta(m)$	Ref.
1680 m/s	0.2 m	12 m	Choi, et al. ⁵
1630 m/s	21.8 m		
1581 m/s	14.5 m	19 m	Jiang, et al. ⁶
1602 m/s	7.4 m		
1605 m/s	21 m	16 m	Jiang, et al. ⁷
1650 m/s	half-space	n/a	Yang, et al. ⁹
1616 m/s	16 m	16 m	this work

water-sediment interface is transmitted into the sediment and can interact, under certain conditions, with subsurficial layers to the extent they exist.

The particular environment used in this discussion is from the Shallow Water 2006 (SW06) experiment off the New Jersey Coast. The sediment structure of this site has been the focus of a number of studies, a majority of which agree on a two layer model where a sediment layer (thickness ~ 20 m) overlays an strong impedance contrast layer (referred to as the R-reflector). The presence of this layer and underlying reflector is directly visible in chirp-sonar profiling data.¹² Results from a number of geo-acoustic inversion studies from this site, centered at 39.0245° N, 73.0377° W, are summarized in Table I.

A. Experimental description

The data used in this discussion was recorded on a moored vertical line array (MORAY) located at the aforementioned coordinates. A source (ITC-2010) positioned within 5 m of the bottom was towed from the stern of the R/V *Knorr* starting at range 50 m from the MORAY and proceeding to range 300 m. The ship traveled at a speed of 0.1 m/s along four different source-receiver bearings while the source transmitted a sequence of three pulses every 12 seconds; a 2-16kHz FM sweep, a 2 ms CW, and then a 3 ms CW, each CW with center frequency 1 kHz. The hydrophone pair (separation 20 cm) centered at the depth 49 m is used to compute the approximate degree of circularity, $\tilde{\Theta}$. The two, 1 kHz cw pulses are utilized for the Θ calculations, while the matched-filtered FM sweep data provides information on the arrival structure. The GPS coordinates of the source were recorded for each transmission.

Figure 3 shows the geometry of the experiment; the ray-paths of the first three arrivals are shown for a source-

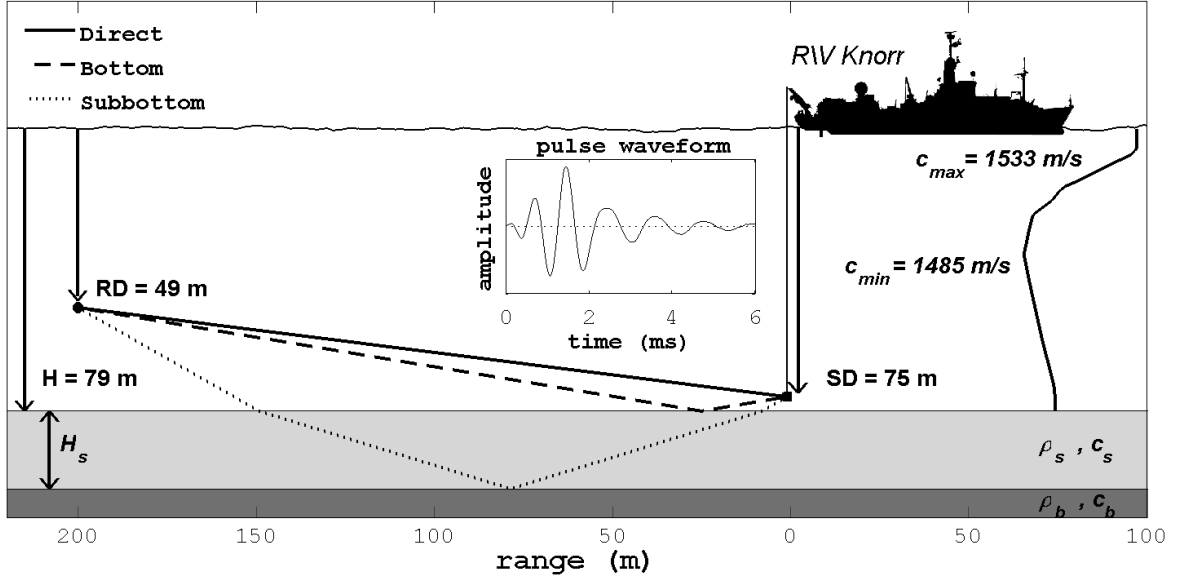


FIG. 3. The experimental geometry and the first three arrivals. The direct (solid), bottom (dashed), and subbottom (dotted) path from the towed source (depth 75 m) to receiving array (depth 49 m) are shown for a source range of 200 m. The sound speed profile in the water column varies from a maximum of 1533 m/s at the surface to a minimum 1485 m/s at the thermocline at 20 m depth, the sound speed at the water-sediment interface is 1499 m/s.

receiver range of 200 m. Although the amplitude of the sub-bottom reflection (dotted line) is substantially weaker than the direct (solid line) and bottom (dashed line) arrivals, the interference caused by this arrival can be observed in the experimental data. The arrival times of these first three paths, extracted from the matched-filtered arrivals of the FM-sweep pulse, show that the direct, bottom and sub-bottom path arrive simultaneously at a range of 200 m. In addition to the matched-filtered data, the measured Θ exhibits a range-dependence that we show corresponds to the arrival angle of the sub-bottom path.

B. PE simulations of Θ for the SW06 site

Broadband parabolic equation (PE) simulations of the SW06 site (computed via the RAM-PE numerical code) demonstrate the effect of the sub-bottom layer on the degree of circularity. The bottom model used in the simulations presented in Fig. 4 consists of 2 layers: the upper layer properties are $c_s=1614$ m/s, $\rho_s = 2000$ kg/m³, $H_s=16$ m, the lower R-reflector half-space properties are $c_b=1740$ m/s, $\rho_b = 2200$ kg/m³ (see Fig. 3 for variable definitions). Attenuation in the sediment layer was set to 0.05 dB/m/kHz, and a value of 0.3 dB/m/kHz was used for the absorbing half-space.⁵

The water column sound speed profile, $c_w(z)$, used in the PE simulations is shown in Fig. 3. Time-series of the pressure and particle velocity are computed via Fourier synthesis of the experimental pulse (shown in the inset of 4a), which in turn are used to compute the time series

of I_c and Θ at each range and depth point. The image of Θ in Fig. 4a is constructed by computing the value of Θ at the time of the direct arrival.

At the receiver depth of 49 m (white horizontal line in Fig. 4a) the direct and sub-bottom arrivals do not interfere at ranges < 150 m. The experimental pulse determines this range; for example, were it to have been longer in time (or processing bandwidth decreased), the point at which direct and sub-bottom arrivals begin to interfere would be less than 150 m. Since the interference at ranges less than 150 m consist only of the direct and bottom arrivals, the depth and range dependence of Θ is very similar to that discussed in Sec. II. If there was no layering structure in the sea-bed, this pattern would extend until the range where the surface path begins to interfere with the direct path. (Additional interference due to the surface path can be seen in Fig. 4 at depths less than 5 m.)

Although the interference pattern for range < 150 m contains little information on the bottom properties, the depth and range dependence of Θ relates directly to the source-receiver geometry. The range dependence of Θ is dependent on the angular difference of the interfering arrivals, the smaller the angular difference of the two arrivals, the greater the scale of the range dependence. The range dependence of alternating signed Θ falls somewhere between $[\lambda/2, \infty)$. A model of the range dependence is given in Sec. V. The greater the difference of the interfering arrival angles, the less sensitive the range dependence of Θ is small changes in the arrival angles, as could be caused by source-depth fluctuation. Note, the

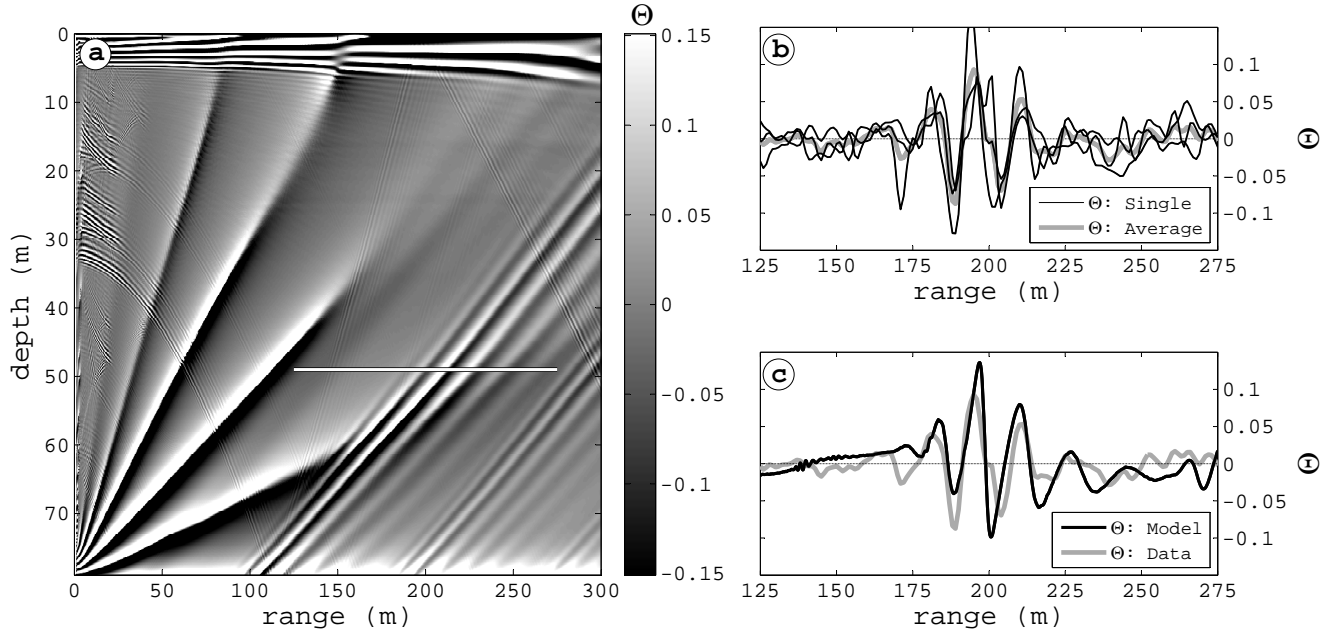


FIG. 4. (a) Image of broad-band PE simulated value of Θ occurring during the direct path arrival as a function of range and depth. See text for bottom model. The range corresponding to the experimental data is shown by white horizontal line at the depth of 49 m. (b) Plot of experimentally measured Θ over three tracks (thin black) and their average (thick gray). (c) Plot of the corresponding model data (thick black) and the averaged data (thick gray) from (b).

bottom-direct-path interference pattern is very sensitive to changes in source depth as the angular difference between these two arrivals approaches zero with increasing range.

C. Experimental measurements of $\tilde{\Theta}$ at the SW06 site

As a result of the ship motion over the course of the experiment, the interference pattern of the direct and bottom arrival are not consistent over the experimental runs. A shallower or deeper source-depth will expand or contract the angular difference of the direct and bottom arrival. Since the angular difference of these paths are close to zero, the fluctuations in angular difference are on the order of the angular difference, which drastically changes the range of the interference nodes effectively smearing out this interference pattern. The interference pattern due to the sub-bottom arrival, however, is stable over the experimental runs. This insensitivity to source depth fluctuation is due to the fact that the propagation angle of the sub-bottom path asymptotes to the critical angle with increasing source-receiver range, while the direct and bottom propagation angles converge to be nearly horizontal. Thus, the fluctuations in the angular difference between the sub-bottom path and the direct/bottom path are only a fraction of their total angular difference, which remains near the critical angle with increasing range.

The experimentally measured $\tilde{\Theta}$ at 49 m depth was computed from the pressure and vertical particle velocity (via the finite difference) as outlined in Section II-C.

Figure 4b shows $\tilde{\Theta}$ as a function range, corresponding to the value of $\tilde{\Theta}$ at the time of the direct arrival for the 250, 1 kHz pulses that arrive over the range span shown in Fig. 4a. Results from the individual ship tracks along the bearings 120°, 210°, and 300° (thin black lines) show a similar feature between 175-230 m that remains through averaging (thick gray line). Figure 4c shows the corresponding PE model of Θ (black line) plotted against the averaged experimental data (gray line).

As observed in both the experimental and modeled data, interference between the first three arrivals causes distinct oscillations in Θ as a function of range. At the ranges where the first three paths interfere, the Θ range dependence can be described by a wavelength, λ_{Θ} , defined as the characteristic range between peaks of similar signed values of Θ . The experimental data yields $\lambda_{\Theta} \simeq 16$ m and the value of λ_{Θ} computed from PE simulations of candidate bottom-models are shown in third column of Table I. As with any measurement, the measure of λ_{Θ} is subjected to some level of uncertainty, which effects the confidence in a particular bottom-model.

V. SENSITIVITY OF λ_{Θ} TO BOTTOM PARAMETERS

The measurement of λ_{Θ} from two vertically spaced hydrophones has an inherent degree of uncertainty, $\sigma_{\lambda_{\Theta}}$. This is set by the signal to noise ratio (SNR) and an analysis of PE simulated data with additive Gaussian white noise with SNR of 30 dB, roughly corresponding to that in effect for the field data, puts $\sigma_{\lambda_{\Theta}} \simeq 1.1$ m. Similarly, the standard deviation of λ_{Θ} measured over

the three range-tracks that comprise the experimental data is $\sigma_{\lambda_\Theta} \simeq 1$ m.

A simple relationship can be used to describe λ_Θ by two propagation angles, which we exploit for a discussion of the sensitivity of λ_Θ to the bottom parameters in terms of the Cramer Rao Lower Bound (CRLB) framework. For a pulse with acoustic wavelength ($\lambda = c_w/f$), this relationship is

$$\lambda_\Theta = \frac{\lambda}{\cos \phi_d - \cos \phi_s} \quad (8)$$

where ϕ_d is the propagation angle of the direct path and ϕ_s is the propagation angle of sub-bottom path.

For a given bottom parameterization, ray theory can be used to compute the arrival angles, where the propagation angle of the direct path is readily determined by the source-receiver geometry and the propagation angle of sub-bottom path is constrained by Snell's law. This constraint can be used to construct the geometry of the sub-bottom path which is sensitive to two parameters, the layer thickness (H_s) and the layer soundspeed (c_s); the density and attenuation of the layer do not effect the propagation angles. Note that a more sophisticated ray tracing method may be necessary to compute these angles if the water-column has a significant sound-speed profile. For this analysis, all the paths considered remain below the thermocline (see Fig. 3) and simple geometrical-methods are adequate.

Figure 5a shows the value of λ_Θ for various candidate two layer models $[c_s, H_s]$, for which the sediment below the layer is considered a halfspace with sound speed 1740 m/s. A particular value of λ_Θ is satisfied by a set of $[c_s, H_s]$ parameterizations and additional information must be included to narrow this parameter space.

One piece of information, contained in the data, is the range dependence of the interference pattern. Figure 5b shows contours of range, for which the sub-bottom path and direct path arrival times will be the same. For example, the line identified with 200 gives all combinations of $[c_s, H_s]$ such that there would be simultaneous arrival of sub-bottom and direct paths at range 200 m.

Another piece of information is the two-way travel time (TWT) between the water-sediment interface and the bottom of the layer from chirp sonar surveys which is reported to be $\text{TWT} \simeq 26$ ms.⁶ This TWT, which follows the relationship $\text{TWT} = 2H_s/c_s$, establishes a layer thickness of 21-22 m and layer soundspeed between 1600-1700 m/s. The dashed line in Fig. 5b shows the parameter estimates for a $\text{TWT} \simeq 26$ ms and the curved solid line shows the parameter estimates for a value of $\lambda_\Theta = 16$. Finally, as noted in Sec IV A., the FM sweep data has been matched-filtered to determine the arrival times of the direct and sub-bottom path, which are equal at range 200 m.

A. CRLB of parameter estimates based on Θ

The uncertainty of the bottom parameters based on a value of λ_Θ can be derived from the Fisher information matrix,

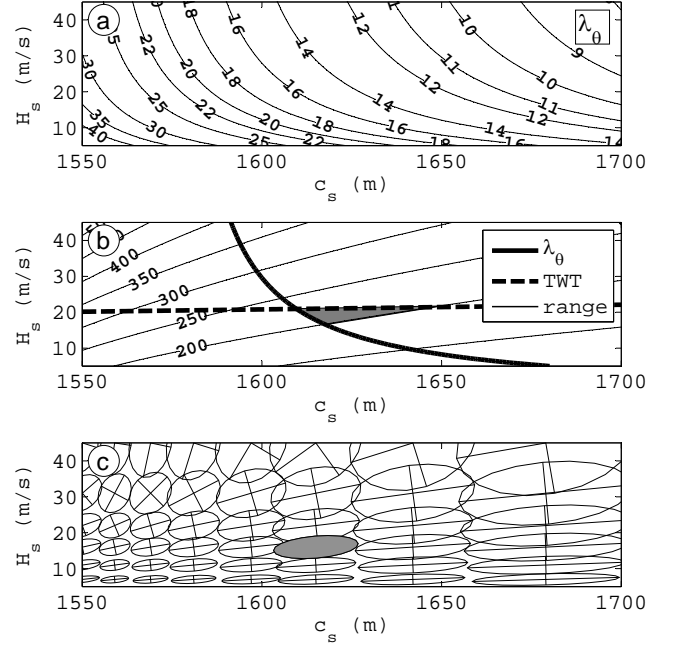


FIG. 5. a) Contours of λ_Θ for the source-receiver geometry shown in Fig. 3. b) Contours of the range where the sub-bottom and direct paths arrive coincidentally. The 200-m contour corresponds to the observation in the data. The solid curved line indicates the parameter set described by the $\lambda_\Theta = 16$ m contour and the dashed line indicates the parameter set from the TWT chirp sonar data. c) The error ellipses representing the CRLB for an uncertainty in the λ_Θ estimate, $\sigma_{\lambda_\Theta} = 1.1$ m. The grayed-filled ellipse corresponds to the uncertainty of the parameters for a best fit, $c_s = 1614$ m/s and $H_s = 16$ m.

$$\mathbf{F} = \frac{1}{\sigma_{\lambda_\Theta}^2} \begin{bmatrix} \frac{\partial^2 \lambda_\Theta}{\partial c_s^2} & \frac{\partial^2 \lambda_\Theta}{\partial c_s \partial H_s} \\ \frac{\partial^2 \lambda_\Theta}{\partial H_s \partial c_s} & \frac{\partial^2 \lambda_\Theta}{\partial H_s^2} \end{bmatrix}, \quad (9)$$

where the elements are the partial derivatives of the λ_Θ with respect to the parameters. The CRLB derived variances and co-variances of the parameter set are computed from the inverse of the \mathbf{F} matrix, \mathbf{F}^{-1} . The eigenvalues of \mathbf{F}^{-1} are the CRLB estimates for the parameters under study. If off-diagonal elements of \mathbf{F}^{-1} are non-zero there is evidently coupling between parameter estimates.

The coupling between these two parameters is shown by the error ellipses in Fig. 5c for a several parameter combinations $[H_s, c_s]$ given $\sigma_{\lambda_\Theta} = 1.15$ m. (The cross of the major and minor axes of the ellipses are centered at $[H_s, c_s]$.) The orientation of the error ellipses, which are determined by the eigenvectors of the \mathbf{F}^{-1} matrix, show that estimates of the two parameters are coupled, and the uncertainty in H_s depends on the uncertainty in c_s . For a thick sediment layer with low sound speed (upper-left corner) the thickness dominates the uncertainty due to the propagation angles being dominated by the geometry, the refraction effect for a small sound-speed contrast is less significant. The refraction effect

becomes more significant as the propagation angles approach the critical angle of the sediment-water interface. For a larger sound speed contrast and a thin sediment layer (bottom-right corner), the sound-speed dominates the uncertainty. Between these two regions, the sensitivity of λ_Θ transitions from thickness dominated to sound speed dominated, where at some point the parameters are equally sensitive. Note that this change in relative sensitivity of the two parameters has implications for adaptive estimation algorithms,¹³ specifically the order in which parameters are estimated.

B. Geo-acoustic inversion results based on λ_Θ

A best-fit parameterization can be constructed from the intersection of the λ_Θ contour with either the 200 m range contour or the chirp-sonar constraint (see Fig. 5b.) Alternatively, another best-fit parameter estimate is one based purely on the TWT constraint and the 200 m range contour. Regardless of the means used to arrive at the best estimate, the best estimate lies somewhere within the triangle of intersecting lines (see shaded region in Fig. 5b).

We conclude that the region defined by the three parameter sets is in agreement with the various parameter estimates in Table I. The best parameter estimate inferred from the towed source transmissions is $H_s = 16 \pm 4$ m and $c_s = 1616 \pm 10$ m/s. The possible values of $[c_s, H_s]$ due to the uncertainty are contained in the filled ellipse in Fig 5c. This error ellipse encompasses the majority of the parameter space given by shaded region in Fig. 5b and we deem this a reasonable best-fit estimate.

VI. SUMMARY AND DISCUSSION

A vector description of the acoustic field contains useful information relating to the propagation of sound. As specifically discussed in this work, the frequency and depth/range dependence of interference patterns can be identified by a vector property which characterizes particle motion, the degree of circularity (Θ). Measurements of Θ are useful in that the range, depth and frequency dependence of Θ :

- relates directly to source and receiver position, having utility in source localization
- relates directly to reflections from sediment layers, having utility in geo-acoustic inversion
- can be approximated in the vertical plane by a vertical line array of hydrophones, and thus can be applied to conventional pressure-based measurement systems

Furthermore, in addition to pressure-based algorithms used in localization and geo-acoustic inversion, the output of vector sensors can be presented in light of vector properties of the sound field.

The results of the geo-acoustic inversion based on a the range dependence of Θ presented here are in agreement with previously reported pressure-based inversion results of the SW06 site. Although this parameterization is consistent with the layered bottom models presented in the literature, one study does suggest a half-space model.⁹ It is worth noting that the circularity data collected along the same 30° bearing could not be distinguished from the noise. As the inversion technique presented here depends on the spatial dependence of particle motion circularity, the lack of a signal along this track supports this conclusion of a half space model for this bearing. Nevertheless, the data collected on the other three bearings (radials) support the a sub-bottom reflector model. The observations of circularity accommodate both of these models, and suggests that the detection of sub-bottom layers might be due to the sensitivity of the measurement system, such as the signal to noise ratio.

The SNR of the circularity is dependent on the background noise of both the pressure field and the particle velocity field. The uncertainty in the Θ measurements could be much improved upon by changing the sensing technique, as the approximate technique used here is subject to the SNR of the pressure field. The background noise measured by an accelerometer is inherently different than the noise on a hydrophone. Depending on the relative SNR of the pressure or particle velocity field, the calculation of Θ via a particle motion sensor may be result in a higher SNR, and thus lower uncertainty in the characteristic scales of Θ . Under the same environmental conditions, this improvement in SNR will reduce the uncertainty in parameter estimates over those derived from pressure-based formulations of circularity.

Acknowledgments

This work is supported by the Office of Naval Research (ONR), Ocean Acoustics Program (Dahl), and the ONR Graduate Trainee Fellowship (Dall'Osto).

- ¹ Thode, A., J. Skinner, P. Scott, J. Roswell, J. Straley, and K. Folkert, "Tracking sperm whales with a towed acoustic vector sensor," *J. Acoust. Soc. Am.* Volume 128, Issue 5, pp. 2681-2694 (2010).
- ² Santos, P., Rodriguez O.C., Felisberto P., Jesus S.M., "Seabed geoacoustic characterization with a vector sensor array," *J. Acoust. Soc. Am.* Volume 128, Issue 5, pp. 2652-2663 (2010).
- ³ D'Spain, G. L., J. C. Luby, G. R. Wilson, and R. A. Gramann, "Vector sensors and vector sensor line arrays: Comments on optimal array gain and detection," *J. Acoust. Soc. Am.* 120 171 (2006).
- ⁴ D'Spain, G. L. "Polarization of Acoustic Particle Motion in the Ocean and its Relation to Vector Acoustic Intensity," 2nd International Workshop on Acoust. Eng. and Tech., Harbin, China (1999).
- ⁵ Choi, J. W., P. H. Dahl and John Goff, "Observations of the R reflector and sediment interface reflection at the Shallow Water '06 Central Site," *J. Acoust. Soc. Am.* 124, EL128-EL134 (2008).

- ⁶ Jiang, Y. M., N. R. Chapman, P. Gerstoft, "Estimation of the Geoacoustic Properties of Marine Sediment Using a Hybrid Differential Evolution Inversion Method," IEEE J. of Oceanic Eng. Vol. 35, No.1 (2010).
- ⁷ Jiang, Y. M., N. R. Chapman and P. Gerstoft, "Short range travel time geoacoustic inversion with vertical line array," J. Acoust. Soc. Am. 124, EL135-EL140 (2008).
- ⁸ Wilmut, M. J., N. R. Chapman, G. J. Heard and G. R. Ebbeson, "Inversion of Lloyd Mirror Field for Determining a Sources Track," IEEE J. of Oceanic Eng. Vol. 32, No. 4 (2007).
- ⁹ Yang, J., D.R. Jackson, and D.J. Tang, "Mid-frequency geoacoustic inversion using bottom loss data from the Shallow Water 2000 Experiment," J. Acoust. Soc. Am. 131 1711-1721 (2012).
- ¹⁰ Dall'Osto, D.R., P.H. Dahl, and J.W. Choi, "Properties of the acoustic intensity vector field in a shallow water waveguide," J. Acoust. Soc. Am. 131(3): 2023-35 (2012).
- ¹¹ Godin, O. A. "Low-frequency sound transmission through a gasliquid interface," J. Acoust. Soc. Am. 123 (4),1866-1879 (2008).
- ¹² Ballard, M. S., K. M. Becker, J. A. Goff, "Geoacoustic inversion for the New Jersey Shelf: 3-D Sediment Model," IEEE J. of Oceanic Eng., Vol. 35, No. 1. (2010).
- ¹³ Schmidt, H. and A. B. Baggeroer, "Physics-imposed resolution and robustness issues in seismo-acoustic parameter inversion," Full Field Inversion Methods in Ocean and Seismo-Acoustics, 85-90 (1995).

Properties of the acoustic intensity vector field in a shallow water waveguide

David R. Dall'Osto^{a)} and Peter H. Dahl

*Mechanical Engineering and Applied Physics Laboratory, University of Washington–Seattle,
1013 NE 40th Street, Seattle, Washington 98105*

Jee Woong Choi

*Department of Environmental Marine Sciences, Hanyang University, 55 Hanyangdaehak-ro, Sangnok-gu,
Ansan, Gyeonggi-do 426-791, Korea*

(Received 27 April 2011; revised 3 November 2011; accepted 13 January 2012)

Acoustic intensity is a vector quantity described by collocated measurements of acoustic pressure and particle velocity. In an ocean waveguide, the interaction among multipath arrivals of propagating wavefronts manifests unique behavior in the acoustic intensity. The instantaneous intensity, or energy flux, contains two components: a propagating and non-propagating energy flux. The instantaneous intensity is described by the time-dependent complex intensity, where the propagating and non-propagating energy fluxes are modulated by the active and reactive intensity envelopes, respectively. Properties of complex intensity are observed in data collected on a vertical line array during the transverse acoustic variability experiment (TAVEX) that took place in August of 2008, 17 km northeast of the Ieodo ocean research station in the East China Sea, 63 m depth. Parabolic equation (PE) simulations of the TAVEX waveguide supplement the experimental data set and provide a detailed analysis of the spatial structure of the complex intensity. A normalized intensity quantity, the pressure-intensity index, is used to describe features of the complex intensity which have a functional relationship between range and frequency, related to the waveguide invariant. The waveguide invariant is used to describe the spatial structure of intensity in the TAVEX waveguide using data taken at discrete ranges. © 2012 Acoustical Society of America.

[DOI: 10.1121/1.3682063]

PACS number(s): 43.30.Yj, 43.30.Bp, 43.58.Fm [AJZ]

Pages: 2023–2035

I. INTRODUCTION

The measurement of an acoustic intensity vector field is a standard technique used for localizing sources and determining sound power.¹ For example, active intensity is the net acoustic power per unit area; measurements of the component normal to a control surface surrounding a source upon integration yields the radiated power. The scaled range $kr \gg 1$, where k is the acoustic wavenumber and r is range from source, provides one kind of far field definition which upon being satisfied the radiation impedance becomes purely real and intensity is considered active. This is most readily seen in the case of a point source where the radiation impedance equals $\rho_0 c(1 + i/kr)$, where ρ_0 is the density and c is the sound speed of the medium.

In a waveguide, just as in room acoustics² and other non-free field environments involving multipath propagation, a scaled range $kr \gg 1$ does not necessarily define a range beyond which the radiation impedance is purely real and this has implications on the intensity vector field. In this paper, properties of the acoustic intensity vector field in a shallow water waveguide are studied, using a combination of field data obtained from an experiment staged off the

coast of Korea within the East China Sea, and synthetic data generated by parabolic equation (PE) simulations.

The paper is organized as follows. Section II establishes the definitions (and notation) for instantaneous and complex intensity to be used in this paper, including the real (active) and imaginary (reactive) parts of complex intensity. Section III describes the field experiment and presents examples of both instantaneous and complex intensities estimated from a vertical line array used in the field experiment. This section ends with a discussion on processing bandwidth and its relation to estimating complex intensity.

In Sec. IV the focus turns to narrow band intensity, or intensity estimated in the frequency domain. Following the work of Eliseevnin *et al.*,³ a Pekeris waveguide model is used to obtain some initial insights into the vector intensity properties of ocean waveguides, where this paper extends their analytic analysis to normalized forms of the complex acoustic intensity vector. In this section experimental data is again examined but with sufficiently narrow bandwidth such that intensity properties lose their time dependence. Using a measured sound speed profile (SSP) and an empirically derived geoacoustic model for the seabed, equivalent synthetic results are generated with PE simulation; properties of the active and reactive intensities observed in both the field and synthetic data are discussed and interpreted. Part of this interpretation includes utilization of the waveguide invariant, as demonstrated for reactive intensity in D'Spain *et al.*,⁴ for particle velocity and active intensity in Ren *et al.*,⁵ and demonstrated in this paper for both active and

^{a)}Author to whom correspondence should be addressed. Electronic mail: dallosto@u.washington.edu

reactive normalized intensity quantities. A summary is provided in Sec. V.

II. ACOUSTIC INTENSITY

Instantaneous acoustic intensity, $S(t)$, also referred to as the Umov–Poynting vector,⁶ describes the instantaneous flow of energy in an acoustic field. To estimate $S(t)$ requires measurement of both the pressure and particle motion at a field point. This quantity can easily be formulated from the output of a vector sensor, a combined receiver measuring the acoustic particle velocity and pressure. The acoustic particle velocity can also be formulated by a spatial distribution of closely spaced pressure sensors, with respect to the signal wavelength.⁷ The equivalence of these measurement systems relies on the fact that in Euler's equation

$$\nabla p(t) = -\rho_0 \mathbf{a}(t), \quad (1)$$

where \mathbf{a} is the particle acceleration and p is the acoustic pressure, the pressure gradient can be approximated along the axis of two pressure sensors using the finite difference of the pressure measurements. The particle velocity, \mathbf{v} , is obtained by time integration

$$\mathbf{v}(t) = - \int_0^t \frac{\nabla p(t')}{\rho_0} dt'. \quad (2)$$

The lower limit in this case represents the onset of the pressure signal.

The instantaneous acoustic intensity is defined by the product of real-valued acoustic pressure and particle velocity. For complex representations, $S(t)$ is defined at a field point using the real parts of these quantities as in

$$S(t) = \text{Re}\{p(t)\}\text{Re}\{\mathbf{v}(t)\}. \quad (3)$$

Note that complex representations $p(t)$ and $\mathbf{v}(t)$ can be generated from their measured real-valued counterparts, $p_M(t)$ and $\mathbf{v}_M(t)$, by using the Hilbert transform of the real-valued signal as discussed further below.

The instantaneous energy flux through a fluid parcel consists of the sum of two components, active and reactive intensity. Active intensity is a measure of the energy flux propagating through a volume and corresponds to the degree to which the pressure and particle velocity signals are in-phase. The time-average of the active intensity represents the mean energy flow. Reactive intensity is the energy flux which in a time-average sense is zero. The existence of reactive intensity depends on the degree to which the pressure and particle velocity signals are out of phase.

The phase properties of an acoustic signal are effectively described using the Hilbert-transform pair to form an analytic signal, consisting of the original time-series [$p_M(t)$ and $\mathbf{v}_M(t)$] and an imaginary component that is 90° out of phase, or phase-quadrature. The analytic pressure signal is

$$p(t) = p_M(t) + i\hat{p}_M(t) \quad (4)$$

and particle velocity signal is

$$\mathbf{v}(t) = \mathbf{v}_M(t) + i\hat{\mathbf{v}}_M(t), \quad (5)$$

where the carrot represents the Hilbert transformed time-series. These can in turn be used to construct the complex intensity,

$$\mathbf{I}_c(t) = \frac{1}{2} p(t) \mathbf{v}^*(t), \quad (6)$$

where the asterisk in this equation denotes the complex conjugate. The complex intensity, as formulated by Heyser,⁸ and as used in Eq. (6), is a time dependent quantity. This differs from a frequency transformed formulation of complex intensity, which is a time-independent definition often described in acoustic intensity literature. The real part of the complex intensity represents the envelope of the active intensity

$$\mathbf{I}(t) = \text{Re}\{\mathbf{I}_c(t)\}, \quad (7)$$

and the imaginary part represents the envelope of reactive intensity

$$\mathbf{Q}(t) = \text{Im}\{\mathbf{I}_c(t)\}. \quad (8)$$

These intensity envelopes represent the low-pass filtered active and reactive intensity components.⁹ Provided the bandwidth B is sufficiently narrow with respect to the center frequency, f_0 , such that $B/f_0 \ll 1$, then $S(t)$ can be represented by the sum

$$S(t) = \mathbf{I}(t) \cos^2[2\pi f_0 t] + \mathbf{Q}(t) \sin[4\pi f_0 t]/2. \quad (9)$$

Properties of $S(t)$ described by Eq. (9) are, for example, readily observed in the instantaneous axial intensity originating from a speaker¹⁰ in free field conditions; for $kr \gg 1$ narrow band measurements (here third-octave band, centered at $f_0 = 250$ Hz) go as $\cos^2[2\pi f_0 t]$ modulated by $\mathbf{I}(t)$, which traces time variation in the source power. The acoustic intensity field in this region is active and the time-average $\langle S(t) \rangle$ is non-zero. For $kr \ll 1$ the instantaneous intensity goes as $\sin[4\pi f_0 t]/2$ modulated by $\mathbf{Q}(t)$, and here the field is reactive and $\langle S(t) \rangle$ is nearly zero. For intermediate kr , the intensity behavior is a combination of these two fields. While this behavior as a function of kr exists in free field conditions, multipath interference in a waveguide represents a source of reactive intensity that exists even for large kr .

III. EXPERIMENTAL DATA SET

The experiment was conducted 17 km northeast of the Korean ocean research station (Jeodo) in waters 63 m deep, and formed a component of a larger program known as the transverse acoustic variability experiment (TAVEX). Acoustic pressure data were collected on a 16-element vertical line array (VLA) with uniform hydrophone spacing (d) of 3 m. Each hydrophone was sampled at a rate of 20.47 kHz. The source signals were implosions of light bulbs (air volume 700 cm³) at a nominal depth of 40 m off the stern of the R/V *Sunjin*. Due to wind coupling of the research vessel and the resulting relative motion of the vessel with respect to the

water column, the bulb deployment system is suspended at an angle from vertical resulting in bulbs implosion depths estimated to be 37 m. The key feature of the implosion signal is a long-time scale rarefaction signal, followed by a impulsive-like spike in pressure. This sequence (bubble pulse) is repeated every 4.7 ms with an exponential decay, similar to that described by Heard.¹¹

Figure 1(a) shows the locations of the bulb sources relative to the moored VLA. The arrows represent the depth-average current vector during each bulb implosion, inferred from a two week acoustic doppler current profiler (ADCP) record collected within 1 km of the VLA site. Although the current measurements began the day after the acoustic measurements, the daily tidal signal in the ADCP data shifts very little over the two week measurement period, and thus the current properties during the two hour period of the acoustic measurements on August 21, 2008 are inferred.

During the time period of the experiment, the magnitude of the current is ~ 0.6 m/s and slowly shifts direction from NW to N. The VLA is subjected to a depth dependent tilt in the direction of the current. Estimates of the relative receiver locations from ray arrival-times of the four closest sources suggest that the array shape remains relatively constant with respect to the current direction [Fig. 1(b)]. Environmental data from the nearby Ieodo tower indicates a 7 m/s southerly wind, and seas characterized by an rms wave-height (H_{rms}) of 0.475 m. SSPs measured from three expendable bathythermograph (XBT) casts during the experiment show a downward refracting environment.

A. Instantaneous and complex vertical intensity

A reliable estimate of the instantaneous intensity based on the finite difference approximation requires low-pass filtering of the pressure time-series before computing the particle velocity to satisfy d/λ requirements. To demonstrate the behavior of the instantaneous intensity for the first three arrivals, the filter bandwidth must be wide enough to resolve

the time-separated arrivals. Typically, finite difference constraints on frequency for a given sensor spacing are set to meet an acceptable percent error in an unknown acoustic field.

The error for the finite difference approximation is a function of frequency and arrival angle. In situations where the field can be described as locally planar, the finite difference error in particle velocity is

$$e(v_x) = 1 - \frac{2 \sin \left[\frac{kd \sin \theta}{2} \right]}{kd \sin \theta}, \quad (10)$$

and for pressure is

$$e(p) = 1 - \cos \left[\frac{kd \sin \theta}{2} \right]. \quad (11)$$

The error in the intensity component along the axis separating the two sensors is the sum of Eqs. (10) and (11), and only effects the magnitude of intensity.⁹ There is no inherent phase error in estimating pressure and vertical velocity and the existence of reactive intensity should not be attributed to errors in the finite difference technique. Measurements may suffer from other sources of error due to imperfections in the measurement system, such as error in the active intensity due to phase mismatch between two sensors or error in the reactive intensity due to amplitude mismatch between two sensors.¹² Fortunately, the errors discussed here are not an issue when considering simulated data, which in turn validate observations in the experimental data.

By limiting the analysis to propagation angles near broadside (where broadside represents $\theta = 0^\circ$), the finite difference error can be kept below the aliasing frequency, preserving the correct sign of pressure and particle velocity. Here, the aliasing frequency occurs when the sign of the pressure estimate at the midpoint used in the finite difference approximation is no longer preserved, most easily interpreted for an endfire arrival ($\theta = 90^\circ$) when $d = \lambda/2$. Considering wavelengths that are small in comparison to the waveguide depth, ray theory can be employed to determine characteristics of the first three arrivals. Arrival angles of the first three eigenrays for the closest source location (A1), based on the experimental SSP in Fig. 2(a) and shown in Fig. 2(b), correspond to an average finite difference error in intensity at 360 Hz of 2% for the direct path (black), 22% for the surface path (light gray), and 41% for the bottom path (dashed), all below the aliasing frequency. Note that this source range is particularly interesting in that it provides a time-series that exhibits temporal separation between the peak arrivals of the first three acoustic paths as well as a time-series that exhibits multi-path interference.

A simulated pressure times-series of the VLA data for the A1 source is constructed to evaluate the effect of the downward refracting SSP and multi-path interference on the received signal. The simulated time-series, $B = 300$ Hz and $f_0 = 210$ Hz, is generated from a Fourier synthesis of parabolic equation (PE) solutions (these methods are further described in Sec. IV). Figure 2(c) shows contours of $|p|^2$ as a function of time and depth receiver depth. The source/

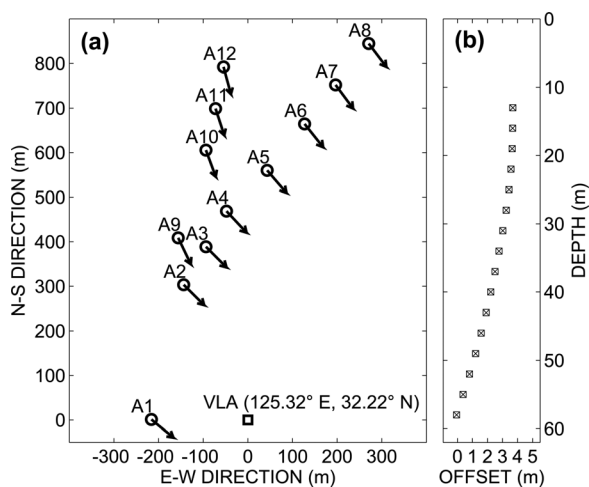


FIG. 1. (a) Source locations (circles) relative to the VLA (square) plotted with their estimated ocean current vector. The labels A1–A12 denote the time sequence of the bulb implosions, occurring over a two hour period. (b) Estimated array shape (relative hydrophone offset) corresponding to a tilt directed along the current vector for each bulb source

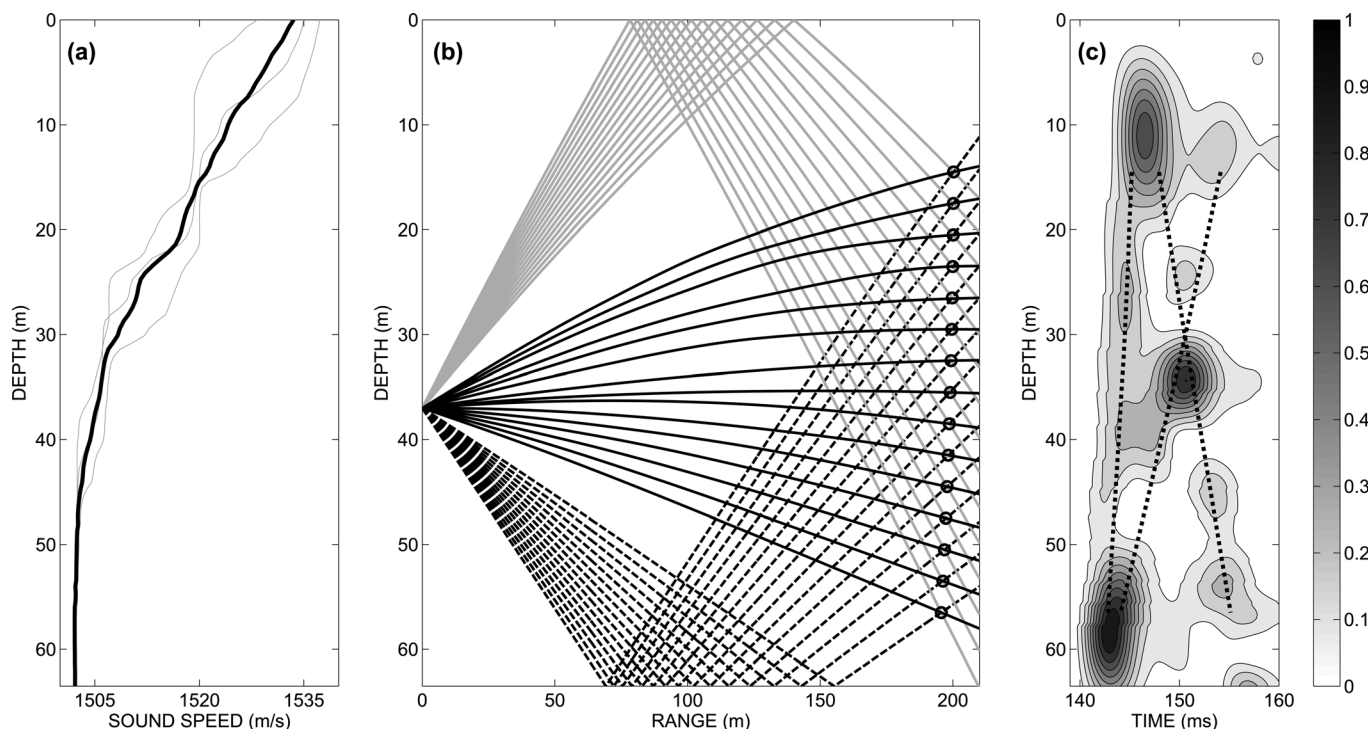


FIG. 2. (a) The average SSP (black) used in numerical simulations is derived from three experimentally measured SSPs (gray). (b) Eigenrays of the direct path (solid black), surface path (gray), and bottom path (dashed) for the midpoints of the 15 hydrophone pairs (circles). (c) Contours of $|p|^2$ of a simulated bulb pulse, $B = 300$ Hz and $f_0 = 210$ Hz, formed by a Fourier synthesis of parabolic equation (PE) numerical solutions. Arrival times of the first three eigenrays (dotted), computed from ray theory, are plotted over the contours.

receiver ranges of the VLA sensors are dependent on the array tilt; the approximate tilt during the A1 signal is incorporated into this simulation. The arrival times of the first three eigenrays are plotted (dotted line) over the contours to highlight the arrival times of these paths. There are two kinds of gradients in $|p|^2$, beyond that accounted for by spherical spreading, observed along the vertical axis of the simulated times series. One is due to constructive and destructive interference due to multi-path interference; the other is due to refraction, owing to the SSP, which generates a focusing and defocussing of the wavefronts. As reactive intensity is directed along decreasing $|p|^2$ contours,⁴ we anticipate a degree of reactive intensity will be observable in these two regions.

With results of Fig. 2 in mind, we now examine the field data. For each pair of neighboring receivers, the instantaneous and complex intensity component directed along the array are formed by Eqs. (3) and (6). In the coordinate system used here, placing the origin at the top of the array (14.5 m), negative intensity indicates propagating energy flux toward the surface. Figures 3(a) and 3(b) show a normalized component of $S(t)$ (dashed lines) computed from the hydrophone pair centered at 32.5 m depth. The hydrophone signals were first processed by a bandpass filter ($B = 300$ Hz and $f_0 = 210$ Hz), which were in turn used to compute the intensity component along the array. These intensity signals are normalized by the maximum squared pressure divided by $\rho_0 c$.

At this depth, the component of $S(t)$ along the array starts off as being predominately negative, as the energy flux associated with the direct path passes the sensors. As the sur-

face reflected and bottom reflected paths arrive at the receiver pair [nearly simultaneously according to the ray arrival times in Fig. 2(c)], the instantaneous intensity becomes oscillatory, i.e., with reduced time average, which is a characteristic of interference between the two paths. If the surface and bottom arrivals were sufficiently time separated, the instantaneous intensity would appear to be on one side of the axis (positive for the surface arrival and negative for the bottom arrival).

The active intensity, normalized in the same manner as the instantaneous intensity, is plotted in Fig. 3(a) over the instantaneous intensity by the thick black line. Similarly the reactive intensity envelope is plotted in Fig. 3(b) as the thick gray line. The negative active intensity indicates energy flux traveling up the array during the direct arrival, which then switches to positive indicating energy flux traveling down the array (away from the surface) during the subsequent arrival. Even though there is energy traveling upwards from the bottom arrival, the signal is dominated by the surface path. The interference between these opposing energy fluxes produces a strong component of reactive intensity.

There also is a small component of reactive intensity associated with the direct arrival observed in the data at 5 ms in Fig. 3(b). This component of reactive intensity may be due to refraction and subsequent focusing associated with the SSP, as seen in contours of $|p|^2$ in the PE simulation in Fig. 2(c). The SSP-dependent focusing, which has the greatest effect on the direct path, does not produce the level of reactive intensity as observed during interference between the surface and bottom paths. The sign of the reactive intensity envelope does not necessarily describe the direction of

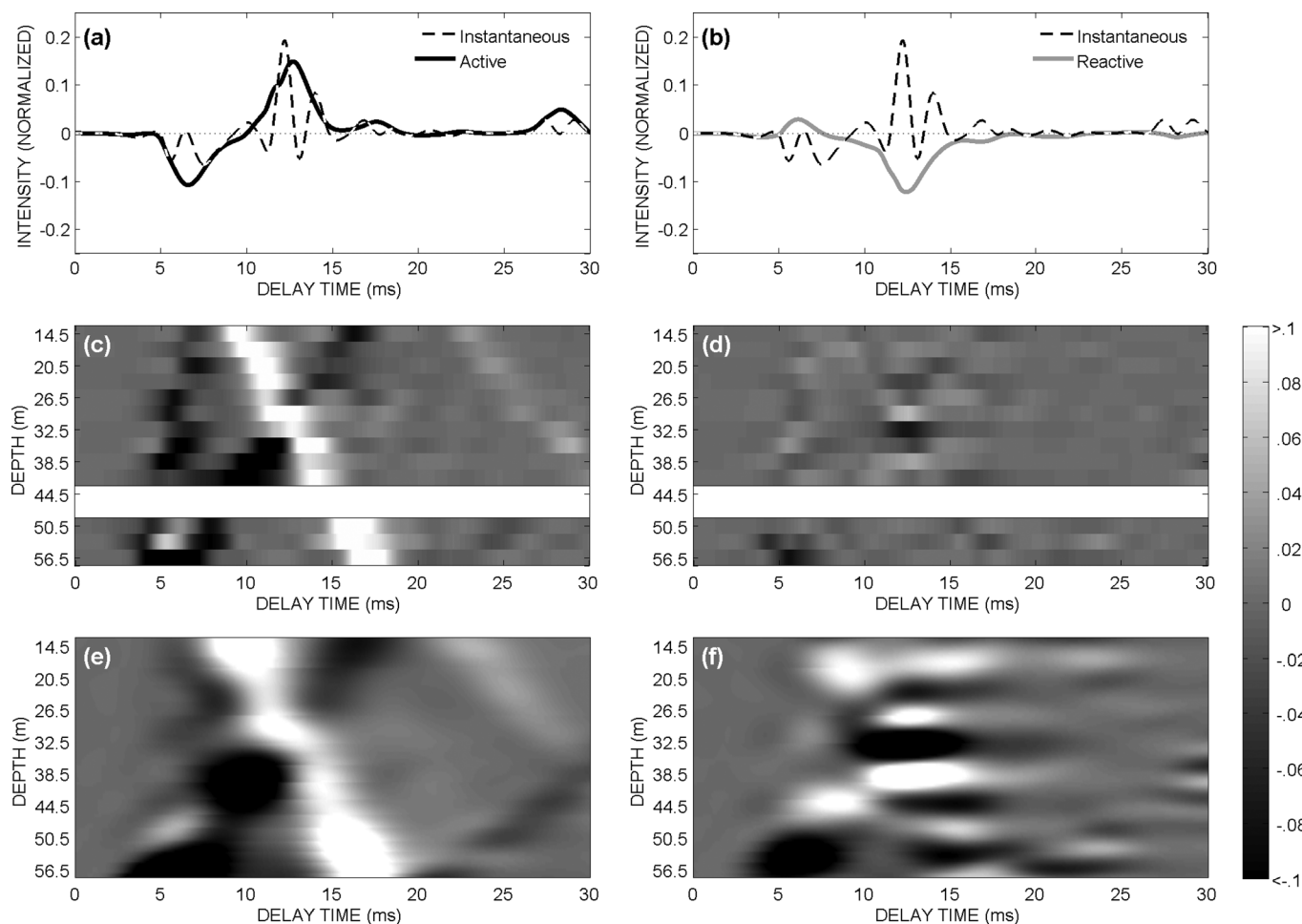


FIG. 3. (a) The component of instantaneous intensity (dashed) and the active intensity envelope (solid black) oriented along the array at depth 32.5 m for the bulb-pulse at 190 m range. (b) The same component of the instantaneous intensity (dashed) plotted over the reactive intensity envelope (solid gray). The intensities are normalized by the maximum value of $|p|^2/\rho_0 c$. (c) Image of the active intensity envelope measured along the length of the array. (d) Image of the reactive intensity envelope measured along the length of the array. Whited out regions correspond to a 6 m gap in data due to an inoperable hydrophone. (e) Image of the active intensity envelope along the modeled VLA array shape for a PE simulated bulb pulse. (f) Image of the corresponding reactive intensity envelope. Active and reactive intensity images are normalized by the depth average of the maximum value of $|p|^2/\rho_0 c$.

the instantaneous energy flux, but it does provide an indication of the proximity and direction of gradients in $|p|^2$.

These intensity features, created from both focusing and multi-path interference, have a spatial structure observable along the length of the VLA. Figures 3(c) and 3(d) show the component of the active and reactive intensity envelopes measured along the array, respectively, for the A1 bulb range. In this case, the intensity envelopes are normalized by a constant equal to the depth average of the maximum magnitude squared pressure divided by $\rho_0 c$. As mentioned earlier, the active intensity envelope denotes the direction of propagating energy flux, negative indicating energy flux up the array toward the surface. Figures 3(e) and 3(f) show the active and reactive intensity envelopes of a simulated bulb-pulse measured along the tilted array. The simulated bulb-pulse is from a Fourier synthesis of PE simulations over a 300 Hz bandwidth, centered at 210 Hz, and shaped by the bulb-signal spectrum. As with the real data, the simulated data show a direct arrival propagating up the array, a surface path down the array and a bottom path traveling up the array but without the degree of granularity inherent in such observations based on large depth separation in the VLA. The spa-

tial structure of the reactive intensity provides information on the interference field.

The direction of the reactive intensity measured along the array gives an indication of the divergence of \mathbf{Q} . In a region about a maxima in the $|p|^2$ field reactive intensity is divergent ($\nabla \cdot \mathbf{Q} > 0$) and \mathbf{Q} points outward from the maxima; maxima are sources of reactive intensity. At minima in the $|p|^2$ field, or nulls, reactive intensity is convergent ($\nabla \cdot \mathbf{Q} < 0$) and \mathbf{Q} points toward the minima; minima are sinks of reactive intensity. In this coordinate system, a change of sign in the reactive intensity component along the array from positive to negative with increasing depth indicates a sink of \mathbf{Q} while a change from negative to positive indicates a source of \mathbf{Q} . The data suggests a sink between 29–33 m and a source between 35–39 m, features created by the constructive and destructive interference of the surface and bottom arrivals. These features are also observed in the simulation. Sinks and sources of reactive intensity are defining characteristics of intensity structures in the waveguide, which are further discussed in Sec. IV.

Note that one possible source of reactive intensity for a time separated surface path occurs when there is substantial

forward scattering from a rough sea surface. The wave conditions and the propagation angles put the Rayleigh parameter, $\chi = 2kH_{\text{rms}} \sin \theta_s$, where θ_s is the angle of the specular reflection relative to the horizontal, equal to 0.36 at the highest frequency (360 Hz). Although χ is less than unity, we expect some degree of forward scattering that could interfere with the reflected surface path and generate reactive intensity.

B. Time averaged complex intensity

At ranges greater than a few waveguide depths, a signal requires a large bandwidth to exhibit time separation between multipaths. The frequency span of the filter applied to the experimental measurements should be set to minimize measurement errors; however, reducing the filter bandwidth has the consequence of reduced time resolution and multipaths are no longer resolved. As the bandwidth is reduced to form an ever more narrowband signal at center frequency f_0 , the complex intensity loses its time dependence and \mathbf{I} and \mathbf{Q} can be represented by a single steady state value (of positive or negative sign) transforming \mathbf{I}_c into a time-independent function of frequency.

It is worth further clarifying the role of bandwidth B in constructing the complex intensity envelope, and subsequent time averaging. Figure 4 illustrates a partitioning of the

300 Hz bandwidth data previously shown in Figs. 3(a)–3(b) into frequency bins located at f_0 by applying filters with a smaller B to the signal. Figures 4(a)–4(c) show examples of the data filtered with $B = 10$ Hz at three different center frequencies, f_0 . Estimates of the component of $\langle \mathbf{I} \rangle$ and $\langle \mathbf{Q} \rangle$ measured along the array from a filter ($B = 10$ Hz) are highly dependent on the center frequency. For example, at $f_0 = 205$ Hz, shown in Fig. 4(b), the component of $\langle \mathbf{I} \rangle \approx 0$ and $\langle \mathbf{Q} \rangle \approx -0.05$ along the array while at $f_0 = 255$ Hz, shown in Fig. 4(c), $\langle \mathbf{I} \rangle \approx 0.03$ and $\langle \mathbf{Q} \rangle \approx 0$. Figure 4(d) shows a summary of $\langle \mathbf{I} \rangle$ and $\langle \mathbf{Q} \rangle$ for the frequency bins spanning the 300 Hz bandwidth. Although the two processing schemes result in very different time series, the sum of $\langle \mathbf{I} \rangle$ and $\langle \mathbf{Q} \rangle$ over the 300 Hz band shown in Fig. 4(d) gives the same estimate of $\langle \mathbf{I} \rangle$ and $\langle \mathbf{Q} \rangle$ from a single 300 Hz bandwidth filter.

The time-average of the active intensity envelope, $\langle \mathbf{I} \rangle$, represents the mean flow of energy and is equivalent to the time-average of instantaneous intensity, $\langle S \rangle$.¹ The time-average of the reactive intensity envelope, $\langle \mathbf{Q} \rangle$, indicates the presence of a non-propagating, oscillatory component of S over the averaging period. This oscillatory component (e.g., here due to multipath interference) depends on the degree to which p and v were not in phase during the averaging period. The time-independent \mathbf{I}_c , as constructed from narrow-band $\langle \mathbf{I} \rangle$ and $\langle \mathbf{Q} \rangle$, is used hereafter to describe the spatial structure of intensity.

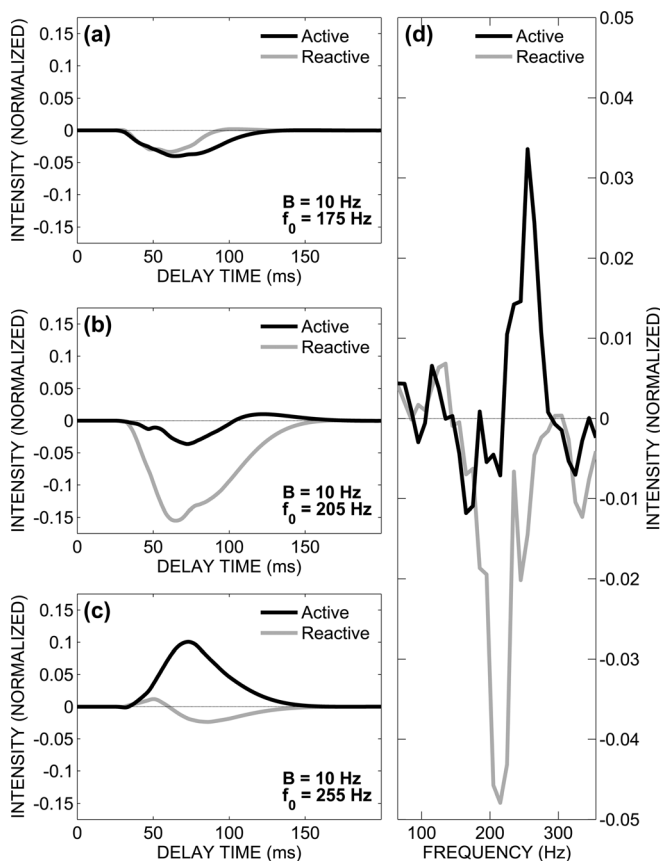


FIG. 4. (a)–(c) Time series of the active (black) and reactive (gray) intensity envelopes at 32.5 m depth for three filters with $B = 10$ Hz at three different center frequencies for the A1 bulb signal (range 190 m). (d) Time-averages of narrow-band filtered signals at 32.5 m depth, $B = 10$ Hz, spanning a 300 Hz band centered at 210 Hz. The intensity quantities here are normalized by the maximum value of $|p|^2/\rho_0 c$ at the corresponding frequency.

IV. SPATIAL STRUCTURE OF INTENSITY IN AN OCEAN WAVEGUIDE

Acoustic intensity in a waveguide will exhibit a spatial structure corresponding to regions of constructive and destructive interference. These structures are characterized by the properties of the time-independent complex intensity and fall into two categories: crests and vortices.

Crests occur in regions of constructive interference where there are maxima in the $|p|^2$ field. In these regions, mean active intensity follows streamlines propagating energy away from the source; a crest follows the most energetic streamline of \mathbf{I} . Constructive interference produces gradients in the $|p|^2$ field, and as $\nabla|p|^2 \propto \mathbf{Q}$, the reactive intensity vector points outward from a particular maximum in the $|p|^2$ field.

Vortices occur in regions of destructive interference where there are minima in the $|p|^2$ field. The mean active intensity forms a vortex, the center of which is a null, or dislocation, where both $|p|^2$ and \mathbf{I}_c are zero. In the vortex region, active intensity can have a left or right-handed curl ($\nabla \times \mathbf{I}$) while reactive intensity converges toward the dislocation. Some experimental and simulated measurements of dislocations are described in D'spain *et al.*⁴

Theoretical work by Eliseevnin *et al.*,³ shows the spatial structure of active intensity for two propagating modes, relating the spatial complexity and strength of the intensity vortices to the difference in mode number. Although the two mode case is useful to visualize intensity structures like the vortex region, the spatial structure of intensity due to two modes is not preserved when considering the complete modal sum.

Additional modes change the interference pattern, e.g., changing the number and location of nulls in the intensity field.

A. Spatial structure of intensity in a Pekeris waveguide

Some additional insight is gained if we examine spatial structure of intensity in the context of a Pekeris waveguide. The complex intensity field of a harmonic source in a Pekeris waveguide can be approximated by the sum of trapped pressure and particle velocity modes. The pressure field is

$$p = \sum_{n=1}^N A_n \Psi_n(z) H_0^{(1)}(k_n r) e^{-i\omega t}, \quad (12)$$

and the horizontal and vertical particle velocities are

$$v_r = \sum_{n=1}^N \frac{-k_n}{i\omega \rho_0} A_n \Psi_n(z) H_1^{(1)}(k_n r) e^{-i\omega t}, \quad (13)$$

$$v_z = \sum_{n=1}^N \frac{1}{i\omega \rho_0} A_n \Phi_n(z) H_0^{(1)}(k_n r) e^{-i\omega t}, \quad (14)$$

where A_n is the modal amplitude, k_n is horizontal wavenumber for the n th mode, and $H_0^{(1)}$ and $H_1^{(1)}$ are the zeroth and first order Hankel functions of the first kind. The mode shapes for the pressure and horizontal particle velocity (Ψ_n) are given by

$$\Psi_n(z) = \sin \left[z \sqrt{k^2 - k_n^2} \right] \quad (15)$$

and the mode shape for the vertical particle velocity (Φ_n) by

$$\Phi_n(z) = \sqrt{k^2 - k_n^2} \cos \left[z \sqrt{k^2 - k_n^2} \right], \quad (16)$$

where the origin of depth coordinate z is at the surface. The modal amplitude¹³ is

$$A_n = \frac{i2\pi P_0 \Psi_n(z_0)}{h - \frac{\Psi_n(2h)}{2\sqrt{k^2 - k_n^2}} + \frac{\rho_0}{\rho_b} \frac{\Psi_n^2(h)}{\sqrt{k_n^2 - \left(\frac{\omega}{c_b}\right)^2}}}, \quad (17)$$

where h is the depth of the water column, z_0 is the source depth, ρ_b and c_b are the density and sound speed of the sediment, and P_0 is the source pressure amplitude defined such that A_n has the dimension of pressure.

The vector components of I_c are found by inserting Eqs. (12)–(14) into Eq. (6). Note that the correct sign of Q depends on the sign convention of the time dependent term, requiring the particular conjugation of Eq. (6) for the ($e^{-i\omega t}$) convention used here.¹⁴

With the Hankel function written in its asymptotic form (valid when $k_n r \gg 1$), $|p|^2$ is given by

$$|p|^2 = \frac{1}{r} \sum_{m=1}^N \sum_{n=1}^N B_m B_n \cos[\Delta\kappa_{mn} r], \quad (18)$$

where $\Delta\kappa_{mn} = k_m - k_n$ and the pressure modal amplitude B_m is

$$B_m = \frac{2A_m \Psi_m(z)}{\pi \sqrt{k_m}}. \quad (19)$$

Simplifying for just two modes, it is seen that Eq. (18) will go to zero (a pressure null or pressure dislocation) at a range and depth combination, such that $\cos[\Delta\kappa_{mn} r] = -1$ when B_m and B_n are of equal sign and magnitude, or $\cos[\Delta\kappa_{mn} r] = 1$ when B_m and B_n are of equal magnitude and opposite sign. A null at one particular depth repeats in range at the interference wavelength, $2\pi/\Delta\kappa_{mn}$.

The active vertical intensity is given by

$$I_z = \frac{1}{r} \sum_{m=1}^N \sum_{n=1}^N B_m C_n \sin[\Delta\kappa_{mn} r], \quad (20)$$

where the vertical velocity modal amplitude C_n is,

$$C_n = \frac{2A_n \Phi_n(z)}{\pi \omega \rho_0 \sqrt{k_n}}. \quad (21)$$

At the range of the pressure null, I_z , again upon simplifying to just two modes, is zero over the entire depth of the water column due to the sine term.

Normalized forms of the complex acoustic intensity, referred to as the pressure intensity indices, which were first introduced by Jacobsen in the context of airborne acoustics,² are applied here to underwater waveguides to assess the nature of the intensity vector field. The pressure intensity index mirrors the complex intensity, with the active pressure intensity index defined as

$$I^* = \frac{I}{|p|^2 / \rho_0 c} \quad (22)$$

and the reactive counterpart defined as

$$Q^* = \frac{Q}{|p|^2 / \rho_0 c}. \quad (23)$$

(The asterisk is used here to indicate that these are normalized intensity quantities, and does not imply a conjugation.) At a pressure null, the characteristics of the vector quantities I^* and Q^* are readily manifested by their vertical components, I_z^* and Q_z^* . It is of interest to examine the behavior of I_z^* as range r approaches such a null location. Continuing with just the two-mode case, expanding Eq. (18) and Eq. (20) about a null range point r_0 shows that their ratio goes as $\pm 1/dr$ where $dr = r - r_0$ and the sign indicates the sense of the curl of the active intensity vortex, the center of which is the null.

In terms of Q_z^* , we first note that at a pressure null, Q_z^* is also zero, and in this case the more interesting property is how the index behaves as a function of z going towards the null. It is worth reiterating that Q_z^* is proportional to the vertical gradient of $|p|^2$. Therefore, a similar expansion of Q_z^* about the null depth point shows that the ratio goes as $1/dz$. This indicates convergence of Q at a null.

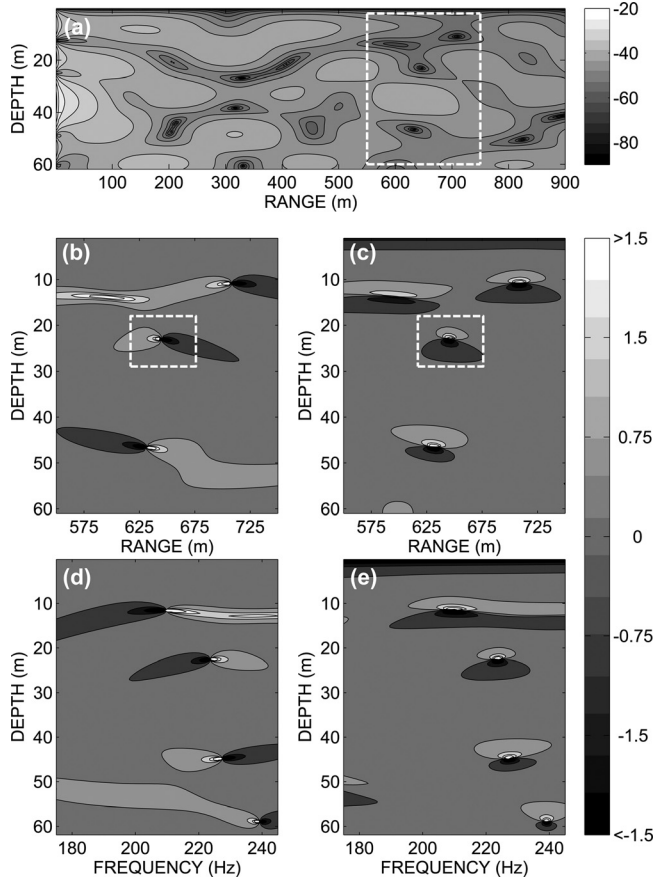


FIG. 5. (a) The narrowband $|p|^2$ field in dB at frequency 210 Hz for a unit point source at 37 m in a Pekeris waveguide. (b) Expanded view of I_z^* and (c) Q_z^* for the white outlined box in (a). (e) I_z^* and (f) Q_z^* plotted as a function of depth and frequency at a fixed range of 650 m.

The behaviors of I_z^* and Q_z^* about a pressure null point for the case of multiple mode propagation have a structure similar to the two mode case. Figure 5(a) shows $|p|^2$ contours for a point source (210 Hz, depth of 35 m) in a Pekeris waveguide, parameterized by depth 62 m, $c_w = 1500$ m/s, $\rho_w = 1024$ kg/m³, overlaying an semi-infinite half-space, with $c_b = 1600$ m/s and $\rho_b = 1600$ kg/m³. The white box outlines a region containing dislocations at a range where the pressure field is sufficiently approximated by six trapped modes.

Contours of I_z^* within the white box in Fig. 5(b) show vortex regions where $|I_z^*| > 1$. The vortex center is indicated by I_z^* changing sign, describing energy flux propagating in opposite directions on either side of the pressure null. Similar contours of Q_z^* [Fig. 5(c)] indicate convergence of reactive intensity at these same null points. The box in Fig. 5(c) shows such a convergence, indicated by Q_z^* changing sign such that Q_z^* is directed inwards toward the center of the null. The behavior of I_z^* along the horizontal axis and Q_z^* along the vertical axis at the nulls show the same abrupt change in sign characterized by the two mode behavior. A key advantage of the index approach is that the pressure intensity indices are maximum at dislocations in the field, and detection of these regions (where $|I_z^*|$ or $|Q_z^*| > 1$) is feasible with one directional component, e.g., Q_z^* and I_z^* as can be provided by a vertical line array.

Finally, Figs. 5(d)–5(e) show I_z^* and Q_z^* , respectively, as a function of depth and frequency at a fixed range (650 m). These form mirror images of the range depth plots in Figs. 5(b), 5(c).

This range and frequency relationship is described by the waveguide invariant, β . Most often applied to the range-frequency relation in $|p|^2$, uses of the β parameter include detection of internal waves,¹⁵ active sonar,¹⁶ passive range estimation,¹⁷ and source localization.¹⁸ The waveguide invariant has also been used to describe the range frequency relationship of the active intensity⁵ and reactive intensity.⁴ We demonstrate next that β also applies to the indices I_z^* and Q_z^* , with the demonstration limited here to the vertical components I_z^* and Q_z^* .

Contours of constant I_z^* in range and frequency are described by

$$\frac{\partial I_z^*}{\partial \omega} d\omega + \frac{\partial I_z^*}{\partial r} dr = 0. \quad (24)$$

Increments of frequency $d\omega$ and range dr where I_z^* has the same contour level are found from

$$\frac{d\omega}{dr} = -\frac{\partial I_z^* / \partial r}{\partial I_z^* / \partial \omega}. \quad (25)$$

In a Pekeris waveguide, I_z^* can be formed from Eq. (18) and Eq. (20) giving

$$I_z^* = \rho_0 c \frac{\sum_{m=1}^N \sum_{n=1}^N B_m C_n \sin[\Delta \kappa_{mn} r]}{\sum_{m=1}^N \sum_{n=1}^N B_m B_n \cos[\Delta \kappa_{mn} r]} = \rho_0 c \frac{\mathcal{N}}{\mathcal{D}}, \quad (26)$$

where \mathcal{N} and \mathcal{D} define the numerator and denominator, respectively. The modal amplitudes B_m and C_m are weak functions of frequency and range independent. This holds for any normal mode description of the acoustic field in a limited bandwidth for which B_m and C_m can be approximated as frequency independent.¹⁶ With this approximation, the right side of Eq. (25) is

$$\frac{\partial I_z^* / \partial r}{\partial I_z^* / \partial \omega} = \frac{\mathcal{D} \frac{\partial \mathcal{N}}{\partial r} - \mathcal{N} \frac{\partial \mathcal{D}}{\partial r}}{\mathcal{D} \frac{\partial \mathcal{N}}{\partial \omega} - \mathcal{N} \frac{\partial \mathcal{D}}{\partial \omega}}. \quad (27)$$

Next, the ratio of the partial derivatives $\mathcal{D}_r / \mathcal{D}_\omega$ is further simplified following arguments given by Brekhovskikh and Lysanov;¹⁹ a demonstration is provided by Quijano *et al.*¹⁶ for striation patterns in $|p|^2$. These arguments also apply to $\mathcal{N}_r / \mathcal{N}_\omega$ which leads to the same simplification, and Eq. (25) thus reduces to the familiar operational relation for β , namely,

$$\beta = \frac{r}{\omega} \frac{d\omega}{dr}. \quad (28)$$

The same functional relationship also applies to Q_z^* .

B. Intensity structure in the TAVEX waveguide

In this section the range-frequency relationship in I_z^* and Q_z^* is examined in the context of the TAVEX waveguide using a combination of field data and parabolic equation (PE) simulation. PE simulations of the complex intensity field for a point source in the TAVEX waveguide allow for finer spatial and frequency resolution of I^* and Q^* .

For the PE simulations, we use the average SSP [Fig. 2(a)] and an experimentally derived bottom model. For the latter, time-separated bottom reflected paths corrected for spreading loss are used to construct an empirical relation for the magnitude of the bottom pressure reflection coefficient (Fig. 6), where spreading loss and arrival angle are derived using ray theory. The representative bottom model (black, dashed line) is defined by $c_b/c_w = 1.06$, density 1600 kg/m^3 and $\alpha_b = 0.019 \text{ dB/m}$, α (the absorption coefficient) applies to the simulation frequency of 210 Hz and originates from a model for averaged properties for sediments in this region.²⁰ We note that historical sedimentological data²¹ and a chirp sonar bottom profile of the experimental site are consistent with the estimated bottom model. The PE simulations of intensity vector properties are carried out by application of finite differencing of a fine spatial sampling. The depth and range computational steps are set to be less than 10% of a wavelength of the maximum simulated frequency.

The time-independent I_c (discussed in Sec. III) is used to construct estimates of I_z^* and Q_z^* with the TAVEX data as a function of frequency based on $B = 1 \text{ Hz}$ with f_0 ranging from 110–310 Hz. For ease in notation, I_z^* and Q_z^* are used to denote the measurement along the VLA, which is influenced by the array tilt discussed in Sec. III. The measurements in fact represent a vector sum of the two directional components according to the tilt of the hydrophone pair used in the intensity formulation. Although the tilt can have a substantial effect on approximating the true value of I_z^* , the horizontal component I_r^* is typically directed away from the source. The direction of the tilt amounts to a positive or negative shift of the approximate I_z^* . The normalized

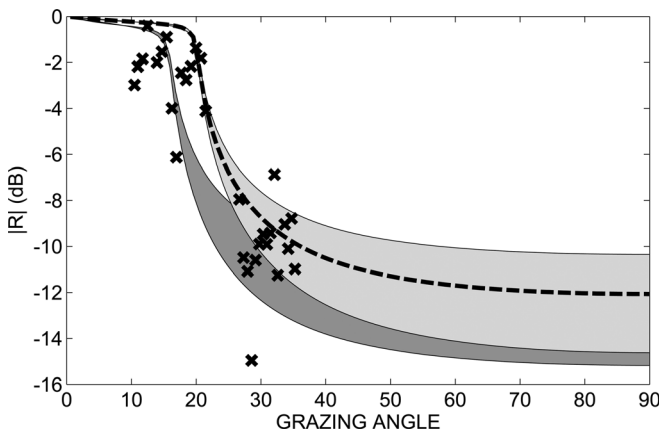


FIG. 6. Estimates of the bottom reflection coefficient (x) for two sound speed ratios $c_b/c_w = 1.04$ (dark gray) and $c_b/c_w = 1.065$ (light gray) over a range of bottom densities 1400 to 1800 kg/m^3 . The representative bottom model (black, dashed) has $c_b/c_w = 1.065$ and $\rho_b = 1600 \text{ kg/m}^3$ and $\alpha_b = 0.019 \text{ dB/m}$.

quantity Q_z^* , on the other hand, is quite robust to errors stemming from array tilt as the horizontal component, Q_r^* , is nearly zero for ranges greater than a few wavelengths. Error in measurement aside, the frequency range relationship described by the waveguide invariant holds for any directional component of I^* and Q^* .

Figures 7(a) and 7(b) show I_z^* and Q_z^* , respectively, as a function of frequency for the 13 vertical intensity receiver depths at the source range (190 m) analyzed in Sec. III. Values where $|I_z^*| > 1$ suggest a dislocation is nearby, but the depth resolution is not adequate to resolve it precisely. The PE simulations of I_z^* [Fig. 7(c)] and Q_z^* [Fig. 7(d)] pinpoint a dislocation at 27 m depth and frequency 187 Hz, indicated by a convergence of Q_z^* in depth when $|Q_z^*| > 1$, in conjunction with $|I_z^*| > 1$. Applying this observation to the data suggests that there is indeed a dislocation between 26 and 33 m depth at frequency 187 Hz as suggested by the combination of $|I_z^*| > 1$ and Q_z^* being convergent, highlighted in the box in Fig. 7(a)–7(b).

It is next of interest to compare the PE simulation as a function of depth and frequency at fixed range 190 m [Figs. 7(c), 7(d)] with one as a function of depth and range at a center frequency 210 Hz [Figs. 7(e), 7(f)]. The center frequency 210 Hz is used here because it corresponds to a peak in the bulb signal spectrum. The figures show that contours of I_z^* and Q_z^* are clearly related in both range and frequency. For this PE simulation, the frequency range relationship follows that of the Eq. (28) with a value of $\beta \approx 1$.

Figure 8 shows the result of PE simulations of the spatial structure of I_z^* and Q_z^* at 210 Hz over the entire range relevant to the TAVEX experiment. A single frequency simulation can be reconstructed by a small set of fixed-range simulations, but at each fixed-range, the simulation is computed over a band of frequencies. The frequency band is then interpreted as a range band according to Eq. (28) using $\beta = 1$. The single frequency I_z^* in Fig. 8(a) is reconstructed in 8(b) by multiple frequency simulations at 24 discrete ranges (separated by the black vertical lines). The single frequency Q_z^* simulation, plotted in Fig. 8(c), is reconstructed in Fig. 8(d). In other words, I_z^* and Q_z^* in Figs. 8(b)–8(d) are computed as a function of frequency between 175 and 245 Hz at discrete ranges spaced every 50 m. The mapping from frequency to range around a center frequency of 210 Hz, and subsequent reconstruction of I_z^* and Q_z^* versus range, display the same intensity spatial structure observed in the original narrow band simulation shown in Figs. 8(a) and 8(c).

The dominant features indicated by I_z^* are dislocations, or nulls, indicated by abrupt changes in sign along “bands” of elevated I_z^* (where $|I_z^*| > 1$). These dislocations often represent a vortex in active intensity, occurring at the point when a band narrows before undergoing an abrupt change in sign. Bands of I_z^* trace out a pattern related to the modal structure of the field. In a two-mode propagation, dislocations repeat at the interference wavelength. In the case of multi-mode propagation, the actual dislocations may not repeat at the interference wavelength, but the bands of I_z^* have a characteristic structure associated with the multiple interference wavelengths as shown in Figs. 8(a), 8(b). Along the bands of I_z^* , there is also a seam of convergence in

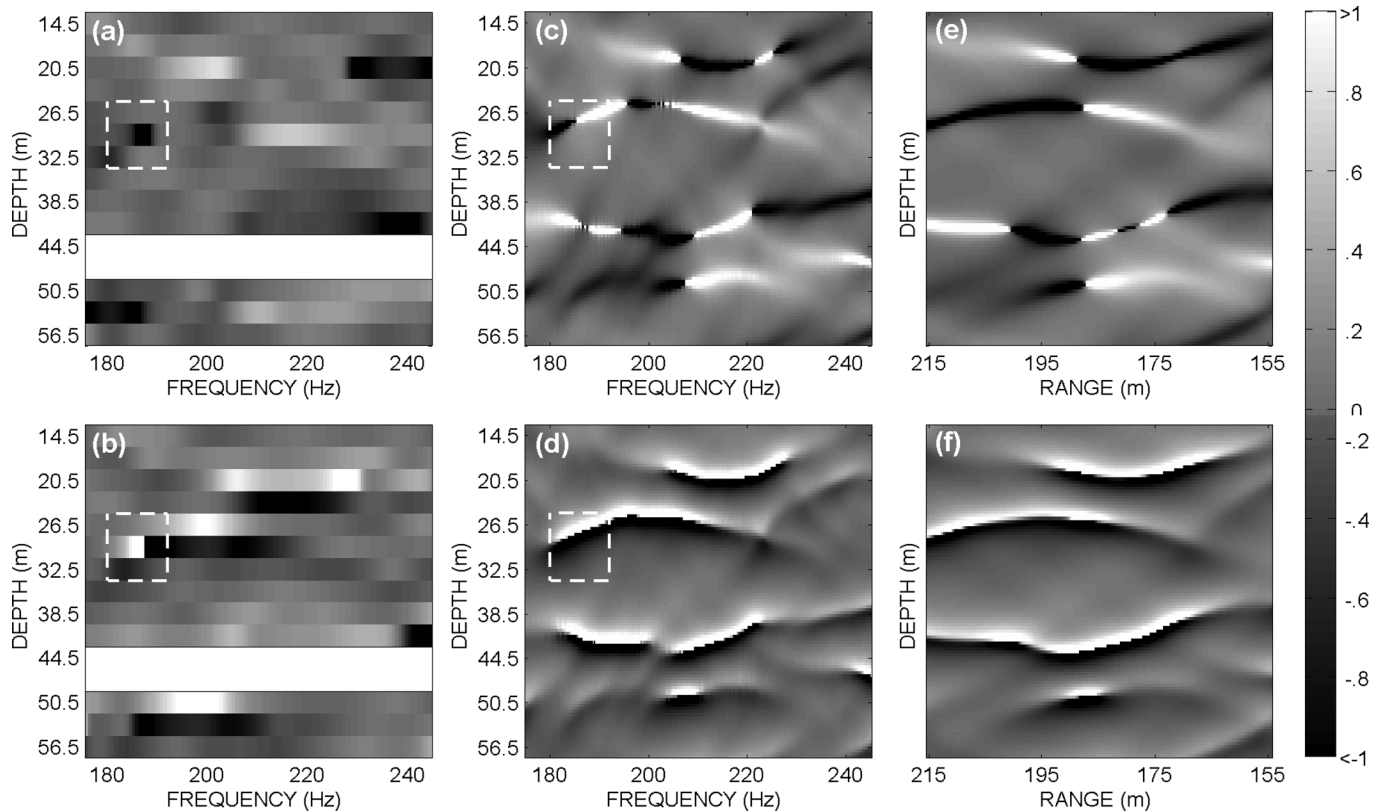


FIG. 7. (a) Experimental estimates of I_z^* as a function of frequency and depth corresponding to the closest bulb range A1; (b) corresponding estimates of Q_z^* . Whited out regions correspond to a 6 m gap in data due to an inoperable hydrophone. (c) PE simulated estimates of I_z^* as a function of frequency and depth at the A1 bulb range (190 m) and based on a source depth of 37 m; (d) corresponding estimates of Q_z^* . The white box highlights a dislocation. (e) PE simulated estimates of I_z^* as function of range and depth at frequency 210 Hz; (f) corresponding estimates of Q_z^* .

reactive intensity, indicated by $Q_z^* > 1$ above and $Q_z^* < 1$ below the seam, or white above black in the in Figs. 8(c), 8(d).

There are some features in the narrowband case which are not perfectly recreated in the mapping. At the interface between two ranges, the curves are not perfectly aligned, which could be attributed to a depth dependence of the β parameter caused by the downward refracting SSP.²² In cases where the sign of I_z^* is opposite, the frequency dependence of the modal amplitudes may come into play, which is neglected when deriving the waveguide invariant.⁴

A similar range frequency relationship of I_z^* and Q_z^* is also observable in the experimental data between two nearby bulb ranges. Figures 9(a) and 9(b) show I_z^* for two sources deployed at A6 (675 m) and A10 (698 m), respectively. Figures 9(c) and 9(d) show the corresponding Q_z^* . The general pattern of pressure intensity indices, as indicated by regions of elevated I_z^* [Fig. 9(a)] and convergent Q_z^* [Fig. 9(c)] (highlighted by the dotted lines) at range 675 m are up-shifted in frequency by ~ 7 Hz at range 698 m. The frequency shift is itself somewhat frequency dependent over the 175–245 Hz range, but the average of 7 Hz puts $\beta \sim 1$. Depth dependence of β is difficult to quantify with this experimental data set due to uncertainties in the source location and possible changes in the relative receiver positions or SSP as the two measurements occur and hour apart.

Continuing with $\beta = 1$, let us use the TAVEX data to reconstruct a nominal image of I_z^* and Q_z^* as a function of range and depth. Using eight discrete ranges corresponding to bulbs deployments A1–A8 and Eq. (28), Figs. 9(e) and 9(f) show the reconstruction of I_z^* and Q_z^* at 210 Hz. Note that closer ranges require a larger frequency span, following Eq. (28), to fill in the gap between sources; a variable frequency range ($d\omega < 2\pi \times 100$ Hz) is employed to accommodate the different range gaps dr associated with A1–A8. Vertical lines in the reconstruction in Figs. 9(e), 9(f) identify a portion of data used. For example, the farthest range between 825 and 950 m is based on data from A8 which represents measurement range 900 m.

There is a degree of ambiguity in the experimental source depth, source range and array shape, and the bottom model used in the PE simulation can be viewed as only approximate. These points must necessarily add to the fact that the ranges corresponding to bulb signals A1–A8 were measured at different times and thus the water column SSP certainly differs slightly for each range. With these limitations in mind, the TAVEX data reconstruction does share some features with the PE simulation, particularly at short ranges. In general, both the data and PE simulation show more bands and seams at ranges less than 500 m than at ranges greater than 500 m. This is because the 500 m range represents a transition of the field into the trapped mode regime. For example, a normal mode solution at frequency 210 Hz (based

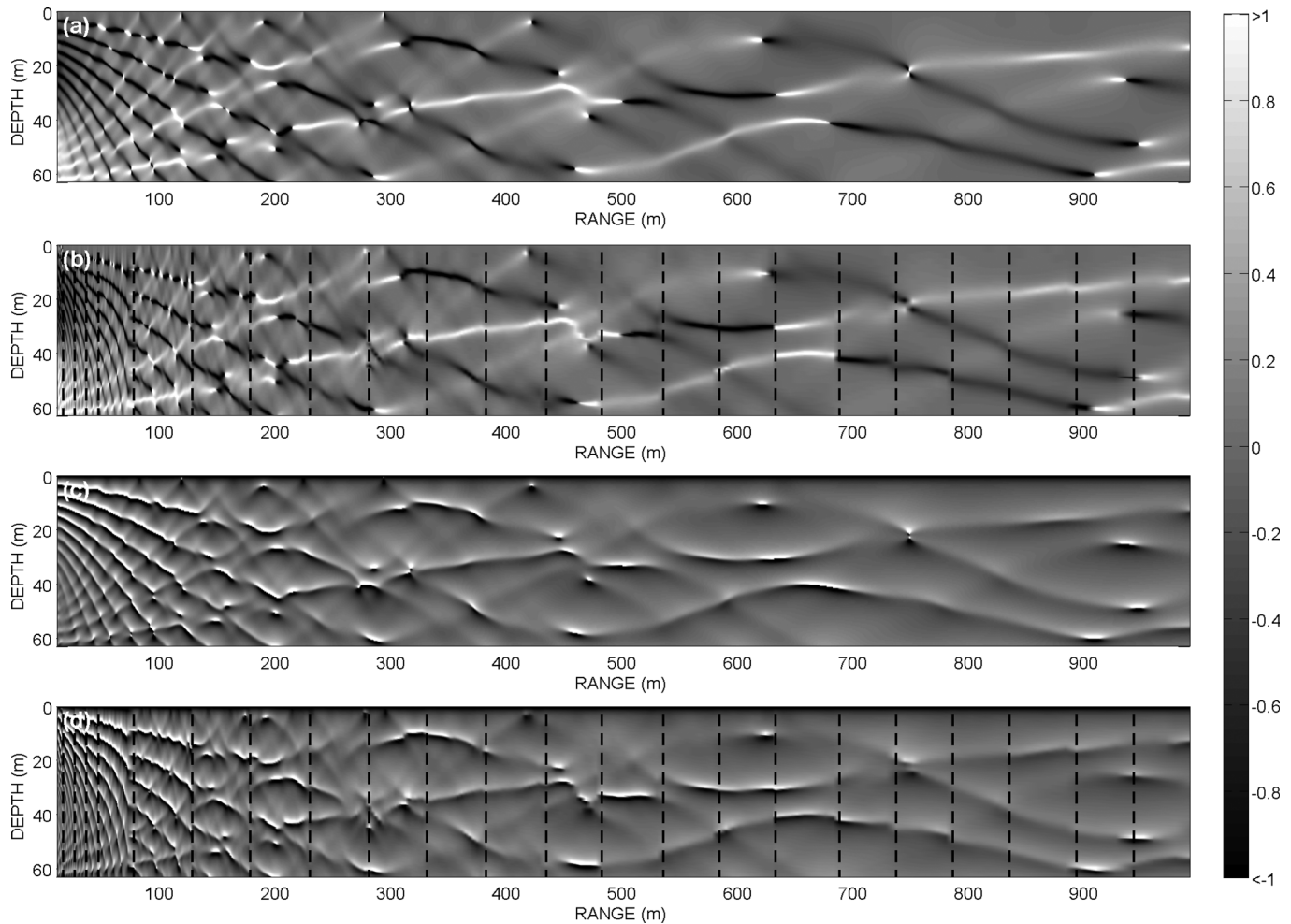


FIG. 8. (a) Single frequency PE simulation of I_z^* at 210 Hz and (b) the reconstruction of I_z^* at 210 Hz from multiple frequency simulations at 24 discrete ranges (separated by dotted vertical lines) using the TAVEX waveguide model (see text). Dislocations are located at the sharp transitions from a large positive value ($I_z^* > 1$) to a large negative value ($I_z^* < -1$). (c) Single frequency PE simulation of Q_z^* at 210 Hz and (d) the reconstruction of Q_z^* at 210 Hz from multiple frequency simulations. The single frequency I_z^* and Q_z^* reconstructions are performed by a mapping of frequency to range using the nominal shallow water waveguide invariant value ($\beta = 1$).

on the same waveguide parameters and computed using the program KRAKEN) is described by six trapped modes and converges to PE simulated field for ranges greater than ~ 500 m.

Finally, regarding the bottom model, we note that small changes in sediment sound speed (~ 10 m/s) change the relative positions of dislocations significantly, an observation that could be exploited for bottom inversion. On the other hand, small changes in sediment density (~ 10 kg/m³) have little effect on I_z^* and Q_z^* . Additional layering in the bottom model can change the position and increase the number of dislocations in the waveguide.

V. SUMMARY

Vector intensity properties in a shallow water waveguide have been studied with experimental and synthetic data. The experimental field data are from acoustic propagation measurements made during an experiment that took place near the Korean ocean research station Ieodo in the East China Sea, in waters 62 m deep. The synthetic data are based on parabolic equation simulations using a geoacoustic model derived from the experimental measurements.

Vector intensity is discussed in the context of real-valued instantaneous intensity $S(t)$ and complex-valued intensity $I_c(t)$. Since the field measurements are made with a vertical line array it is only the vertical component of $S(t)$, and the real and imaginary parts of $I_c(t)$ corresponding to the envelope of active and reactive intensities, respectively, that are described and interpreted. By envelope, we mean a low-passed version of active and reactive intensity without modulation associated with a center frequency. However, it is shown that the vertical components contain most of the waveguide information. In particular, properties of the waveguide are revealed by examining the vertical component of the time-dependent active and reactive intensity envelopes. The complex intensity for time separated multipaths reveals the sign of the propagating vertical energy flux, the degree of multipath interference, and hints at SSP-dependent focusing associated with the direct arrival. Time averages of the active and reactive intensity envelopes allow for comparison of time-domain estimates with a frequency domain representation of complex intensity.

Normalized field indicators, referred to as pressure intensity indices, are described as functions of frequency. The

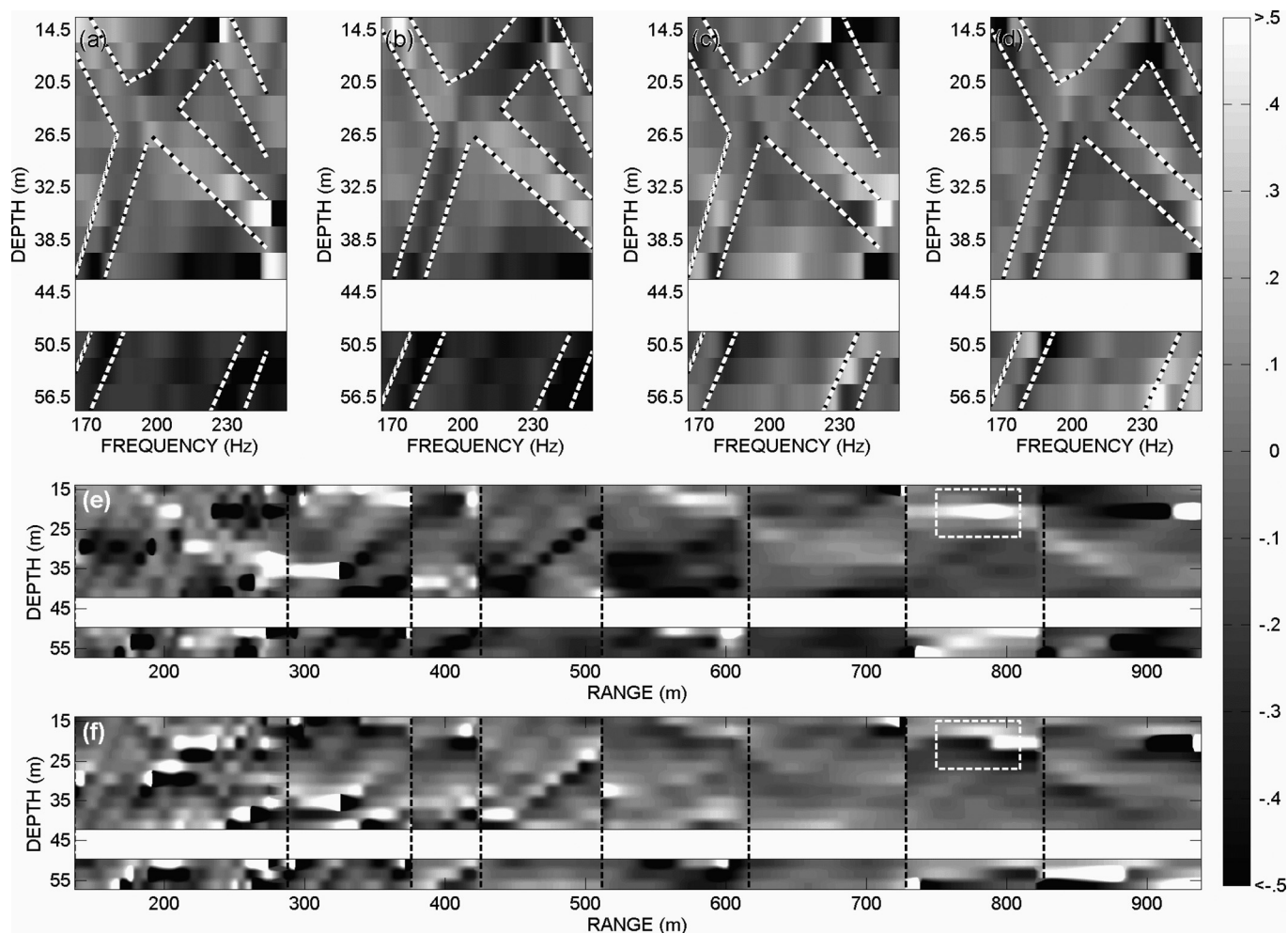


FIG. 9. (a) I_z^* versus depth for bulb A6 (range 675 m); (b) corresponding I_z^* for bulb A10 (range 698 m). (c) Q_z^* versus depth for bulb A6; (d) corresponding Q_z^* for bulb A10. Regions where I_z^* is elevated above the neighboring frequencies and where Q_z^* is convergent are highlighted by dotted lines. Whited out regions correspond to a 6 m gap in data due to an inoperable hydrophone. (e) Eight source-ranges (corresponding to bulb deployment A1–A8) and the waveguide invariant ($\beta = 1$) are used to reconstruct I_z^* at 210 Hz as a function of range at the 13 depths; (f) corresponding Q_z^* .

pressure intensity indices I^* and Q^* indicate two types of intensity structures: crests (regions of constructive interference) and dislocations (nulls from destructive interference). Crests have associated with them a divergence in reactive intensity, whereas nulls have associated with them a convergence in reactive intensity and vortex structure in the active intensity. Crests are indicated by $|I^*| < 1$ and $|Q^*| < 1$ and nulls by $|I^*| > 1$ and $|Q^*| > 1$. The behavior of the index vector magnitude at null structures is describable by the single directional component $|I_z^*| > 1$ and $|Q_z^*| > 1$. The relative location of the null can be described by the sign of the indices; a null occurs where Q_z^* is convergent and where I_z^* undergoes a change in sign.

It was further shown that contours of constant I_z^* and Q_z^* in range and frequency are related by the waveguide invariant, which was then used to map PE simulated frequency data at fixed range to another range for some center frequency. This analysis was repeated with the TAVEX data; in this case a reconstruction of I_z^* and Q_z^* as a function of depth over the entire ~ 1 km range was made using data associated with eight discrete ranges between 200 m and 1 km. The reconstruction has certain limitations based on

uncertainties in the experimental environment and geometry, nevertheless the data reconstruction and the PE simulation displayed some common features.

The formulation of complex intensity and its normalized quantities provide a new look at properties of the sound field that are directly related to waveguide properties. We anticipate that improved knowledge of the vector intensity field in a waveguide will find applications in passive and active sonar, direction-of-arrival sensing, and acoustic inversion studies involving waveguide properties.

ACKNOWLEDGMENTS

This work is supported by the Office of Naval Research (ONR) Ocean Acoustics Program (P.H.D.), the ONR Graduate Trainee Fellowship (D.R.D.), and (for J.W.C.) the Korean Agency for Defense Development (ADD). The authors thank Dr. Altan Turgut and the Naval Research Laboratory (NRL) for the use of the vertical line array during the TAVEX experiment. We also thank the crew of the R/V *Sunjin*, and Dr. Peter Mignerey (NRL), Dr. Seongil Kim (ADD), and Dr. Young-Gyu Kim (ADD) for their overall experimental coordination during TAVEX.

- ¹J. A. Mann III, J. Tichy, and A. J. Romano, "Instantaneous and time averaged energy transfer in acoustic fields," *J. Acoust. Soc. Am.* **82**, 17–30 (1987).
- ²F. Jacobsen, "Sound field indicators: Useful tools," *Noise Control Eng. J.* **35**(1), 41–46 (1990).
- ³V. A. Eliseevnin and Yu I. Tuzhilkin, "Acoustic power flux in a waveguide," *Acoust. Phys.* **47**, 688–694 (2001).
- ⁴G. L. D'Spain, D. P. Williams, G. Rovner, W. A. Kuperman, and the SWARM 95 Team, "Energy flow in interference fields," *Proceedings of Ocean Acoustic Interference Phenomena and Signal Processing* (2002), pp. 171–203.
- ⁵Qun-yan Ren, J.-P. Hermand, and Sheng-chun Piao, "The interference phenomena of broad-band vector field and striation processing," *Proceedings, 4th International Conference and Exhibition on "Underwater Acoustic Measurements: Technologies & Results"* (2011), pp. 905–912.
- ⁶V. A. Shchurov, *Vector Acoustics of the Ocean* (Vladivostok, Dalnauka, 2006), p. 16.
- ⁷Gerald L. D'Spain, James C. Luby, Gary R. Wilson, and Richard A. Graann, "Vector sensors and vector sensor line arrays: Comments on optimal array gain and detection," *J. Acoust. Soc. Am.* **120**, 171–185 (2006).
- ⁸Richard C. Heyser, "Instantaneous intensity," *Proceedings of the 81st Convention of the Audio Engineering Society*, Preprint 2399 (1986).
- ⁹F. J. Fahy, *Sound Intensity*, 2nd ed. (Chapman and Hall, London, 1995), p. 105.
- ¹⁰F. Jacobsen, "A note on instantaneous and time-averaged active and reactive intensity," *J. Sound Vib.* **147**, 489–496 (1991).
- ¹¹G. J. Heard, M. McDonald, N. R. Chapman, and L. Jaschke, "Underwater light bulb implosions: A useful acoustic source," *Oceans'97, MTS/IEEE Conference Proceedings* (6–9 October, 1997), Vol. 2, pp. 755–762.
- ¹²F. Jacobsen, "A note on finite difference estimation of acoustic particle velocity," *J. Sound Vib.* **256**(5), 849–859 (2002).
- ¹³George V. Frisk, *Ocean and Seabed Acoustics: A Theory of Wave Propagation* (Prentice-Hall, Englewood Cliffs, 1994), p. 148.
- ¹⁴F. Jacobsen, "Active and reactive, coherent and incoherent sound fields," *J. Sound Vib.* **130**(3), 493–507 (1989).
- ¹⁵D. Rouseff, "Effects of shallow water internal waves on ocean acoustic striation patterns," *Waves Random Media* **11**, 377–393 (2001).
- ¹⁶Jorge E. Quijano, Lisa M. Zurk, and Daniel Rouseff, "Demonstration of the invariance principle for active sonar," *J. Acoust. Soc. Am.* **123**, 1329–1337 (2008).
- ¹⁷K. L. Cockrell and H. Schmidt, "Passive ranging using the waveguide invariant," *J. Acoust. Soc. Am.* **127**, 2780–2789 (2010).
- ¹⁸A. Turgut, M. Orr, and D. Rouseff, "Broadband source localization using horizontal-beam acoustic intensity striations," *J. Acoust. Soc. Am.* **127**, 73–83 (2010).
- ¹⁹L. M. Brekhovskikh and Y. P. Lysanov, *Fundamentals of Ocean Acoustics*, 3rd ed. (Springer, New York, 2002), p. 142.
- ²⁰Lin Wan, Ji-Xun Zhou, and Peter H. Rogers, "Low-frequency sound speed an attenuation in sandy seabottom from long-range broadband acoustic measurements," *J. Acoust. Soc. Am.* **128**, 578–589 (2010).
- ²¹J. S. Youn and G. W. Go, "Sedimentological characteristics of the surface sediments in the southern sea off Cheju Island, Korea," *J. Oceanological Soc. Korea* **22**(3), 130–142 (1987).
- ²²D. Rouseff and R. C. Spindel, "Modeling the waveguide invariant as a distribution," *Proceedings of Ocean Acoustic Interference Phenomena and Signal Processing* (2002), pp. 137–150.

REPORT DOCUMENTATION PAGE					<i>Form Approved</i> <i>OMB No. 0704-0188</i>	
<small>The public reporting burden for this collection of information is estimated to average 1 hour per response, including the time for reviewing instructions, searching existing data sources, gathering and maintaining the data needed, and completing and reviewing the collection of information. Send comments regarding this burden estimate or any other aspect of this collection of information, including suggestions for reducing the burden, to Department of Defense, Washington Headquarters Services, Directorate for Information Operations and Reports (0704-0188), 1215 Jefferson Davis Highway, Suite 1204, Arlington, VA 22202-4302. Respondents should be aware that notwithstanding any other provision of law, no person shall be subject to any penalty for failing to comply with a collection of information if it does not display a currently valid OMB control number.</small>						
PLEASE DO NOT RETURN YOUR FORM TO THE ABOVE ADDRESS.						
1. REPORT DATE (DD-MM-YYYY) 08-01-2013		2. REPORT TYPE Final Technical Report			3. DATES COVERED (From - To) 01 Jan 2008 - 31 Dec 2012	
4. TITLE AND SUBTITLE Elliptical acoustic particle motion in underwater waveguides					5a. CONTRACT NUMBER	
					5b. GRANT NUMBER N00014-08-1-0297	
					5c. PROGRAM ELEMENT NUMBER	
6. AUTHOR(S) David R. Dall'Osto and Peter H. Dahl, University of Washington					5d. PROJECT NUMBER	
					5e. TASK NUMBER	
					5f. WORK UNIT NUMBER	
7. PERFORMING ORGANIZATION NAME(S) AND ADDRESS(ES) Applied Physics Laboratory University of Washington 1014 NE 40th St. Seattle, WA 98105					8. PERFORMING ORGANIZATION REPORT NUMBER	
9. SPONSORING/MONITORING AGENCY NAME(S) AND ADDRESS(ES) Dr. Robert Headrick, Code 322 Office of Naval Research 875 N. Randolph Street Arlington, VA 22203-1995					10. SPONSOR/MONITOR'S ACRONYM(S) ONR	
					11. SPONSOR/MONITOR'S REPORT NUMBER(S)	
12. DISTRIBUTION/AVAILABILITY STATEMENT Distribution Statement A: Approved for Public Release, Distribution Unlimited						
13. SUPPLEMENTARY NOTES						
14. ABSTRACT <p>The degree of circularity is a vector quantity relating to the acoustic particle motion induced in an acoustic field, and is formulated by measurements of the acoustic particle velocity or the complex vector intensity. It characterizes the ellipticity of the particle motion path that, for example, can arise when there is interference between a source signal and its reflections. In an ocean waveguide the spatial dependence of this vector property depends on the water column sound-speed, surface conditions and bottom properties, in addition to the source/receiver geometry. In waveguides with nearly horizontal boundaries, the vertical component of the instantaneous intensity can be used to provide an approximation to the degree of circularity. This approximation, applied to acoustic pressure measurements from two closely spaced hydrophones made in 2006 off the New Jersey coast in waters 80 m deep, is used to invert for environmental parameters of the sediment structure.</p>						
15. SUBJECT TERMS acoustic particle motion, underwater waveguides, acoustic particle velocity, acoustic pressure measurements						
16. SECURITY CLASSIFICATION OF:			17. LIMITATION OF ABSTRACT U	18. NUMBER OF PAGES 10	19a. NAME OF RESPONSIBLE PERSON David Dall'Osto	
a. REPORT U	b. ABSTRACT U	c. THIS PAGE U			19b. TELEPHONE NUMBER (Include area code) (206) 543-1300	

Reset

Presentations:

- D. R. Dall'Osto and P. H. Dahl, "Underwater vector intensity measurements in the ocean and laboratory," Invited Talk for special session in Sound Intensity for Acoustical Society of America Meeting, Kansas City, MO, Oct 2012
- D. R. Dall'Osto and P. H. Dahl, "The effect of bottom layering on the acoustic vector field," Presentation abstract for Acoustical Society of America Meeting, Kansas City, MO, Oct 2012
- D. R. Dall'Osto, and P. H. Dahl, "Vertical Intensity Properties of the TAVEX waveguide," Presentation abstract for Pacific Rim Underwater Acoustics Conference, 2011, Jeju Island, Korea, Oct. 2011
- D. R. Dall'Osto, and P. H. Dahl, "Coherence of Pressure and Particle Velocity," Presentation abstract for Pacific Rim Underwater Acoustics Conference 2011, Jeju Island, Korea, Oct. 2011
- D. R. Dall'Osto, P. H. Dahl and J. W. Choi, "Vertical intensity structure in a shallow water waveguide," Presentation abstract for Acoustical Society of America Meeting, Seattle, WA, May 2011
- D. R. Dall'Osto and P. H. Dahl, "Airborne noise contributions to the underwater noise sound field," Presentation abstract for Acoustical Society of America Meeting, Seattle, WA, May 2011
- D. R. Dall'Osto and P. H. Dahl, "Implications of signal intensity fluctuations on vector sensor array processing," Presentation abstract for IEEE Oceans 2010 Seattle, WA, September 2010
- D. R. Dall'Osto and P. H. Dahl, "Utilization of the pressure gradient along a sparse vertical line array to determine vertical arrival angle," Presentation abstract for Acoustical Society of America Meeting, Baltimore, MD, May 2010
- D. R. Dall'Osto and P. H. Dahl, "An analysis of the Doppler shifted aircraft noise signature as measured by a hydrophone located within an evanescent field and implication for localization," Presentation abstract for Acoustical Society of America Meeting, Baltimore, MD, May 2010
- D. R. Dall'Osto and P. H. Dahl, "Ambient noise properties in a region of Puget Sound." Presentation abstract for Acoustical Society of America Meeting, Portland, OR, April 2009
- D. R. Dall'Osto and P. H. Dahl, "Environmental noise studies in Puget Sound." Presentation abstract for Acoustical Society of America Meeting, New Orleans, LA, Oct. 2007

Publications:

- D. R. Dall'Osto and P. H. Dahl, "Elliptical particle motion in underwater waveguides." Journal of the Acoustical Society of America: Submitted Jan. 2013
- D. R. Dall'Osto and P. H. Dahl, "Waveguide properties of active intensity vorticity." European Conference on Underwater Acoustics Proceedings, Edinburgh, Scotland, June 2012
- D. R. Dall'Osto, P. H. Dahl and J. W. Choi, "Properties of the acoustic intensity vector field in a shallow

water waveguide." Journal of the Acoustical Society of America, Vol. 131 (3) pp. 2023-2035
March 2012

D. R. Dall'Osto and P. H. Dahl, "Vertical intensity properties of the TAVEX waveguide," Pacific Rim Underwater Acoustics Conference Proceedings, Jeju Island, Korea, Oct. 2011

D. R. Dall'Osto and P. H. Dahl, "Coherence of pressure and particle velocity in SW06 experiments," Pacific Rim Underwater Acoustics Conference Proceedings, Jeju Island, Korea, Oct. 2011

D. R. Dall'Osto and P. H. Dahl, "Implications of signal intensity fluctuations on vector sensor array processing." Proceedings of IEEE Oceans, Seattle, WA, Sept. 2010

D. R. Dall'Osto and P. H. Dahl, "An analysis of the Doppler shifted aircraft noise signature as measured by a hydrophone located within an evanescent field, and implication for source localization." Acoustical Society of America and Noise-Con Proceedings, Baltimore, MD, April 2010